https://doi.org/10.1016/j.expthermflusci.2018.02.033

Unsteady Behavior of a Sweeping Impinging Jet: Time-Resolved Particle Image Velocimetry Measurements

XIN WEN[1,2], YINGZHENG LIU[1,2]*, HUI TANG[3]

[1] Key Lab of Education Ministry for Power Machinery and Engineering
School of Mechanical Engineering, Shanghai Jiao Tong University
800 Dongchuan Road, Shanghai 200240, China

[2] Gas Turbine Research Institute, Shanghai Jiao Tong University
800 Dongchuan Road, Shanghai 200240, China

[3] Department of Mechanical Engineering, The Hong Kong Polytechnic University,
Kowloon, Hong Kong SAR, China

Submitted in February 2018

* Corresponding author.
E-mail address: yzliu@sjtu.edu.cn (Y.Z. Liu)

Abstract

The unsteady behavior of a sweeping impinging jet is measured experimentally using time-resolved particle image velocimetry. For the configuration with a jet-to-wall spacing ratio $L/d_h = 8$, an approximately linear increase in the sweeping frequency is observed with Reynolds numbers (Re) between 2.7×10^3 and 9.3×10^3, especially at high Reynolds numbers. The saturation of the sweeping jet, at which the maximum deflection angle is reached, occurs at $Re = 6.7 \times 10^3$. Special focus is then placed on the spatial and temporal variations of unsteady flow fields at two Reynolds numbers $Re = 4.0 \times 10^3$ and 9.3×10^3. The unsteady behavior in the near-exit region is first compared. At a higher Reynolds number, the jet in the near-exit region remains at the maximum deflection angle for a longer time during one oscillation cycle with more concentrated jet momentum, resulting in a faster switching process. In the near-wall region at $Re = 4.0 \times 10^3$, the sweeping impinging jet exerts a large region of influence due to the oscillation motion of the impact region along the wall. The time-averaged velocity components and velocity fluctuating components near the wall show double peaks on both outer sides and a minimum in the middle of the near-wall region. At $Re = 9.3 \times 10^3$, due to the rapid and intensive sweeping process, the jet column breaks in the near-exit region, resulting in a weak flow in the middle of the near-wall region. Accordingly, the profiles of the time-averaged velocity components and velocity fluctuating components show higher double-peak values but an even lower minimum value. Finally, the state-of-the-art dynamic mode decomposition method is used to capture the main flow behavior of distinct frequencies at these two selected Reynolds numbers. Bounded by the breaking location of the jet column, the flow with a superharmonic oscillation frequency in the middle of the near-wall region disappears at $Re = 9 \times 10^3$. Therefore, the energetic flow patterns are found to be more evenly distributed in the near-exit region than in near-wall region. The phase correlation between the captured flow patterns is determined by projecting the phase-averaged flow fields onto the most energetic modes.

Keywords: Sweeping jet; Impingement; TR-PIV; LIF; DMD.

Nomenclature

A	Linear mapping between flow fields
a_i	Mode coefficients of DMD
C	Companion matrix
d	Diameter of PIV tracking particles
d_h	Hydraulic diameter
f	Oscillation frequency of the sweeping jet
L	Jet-to-plate spacing
$\dot{\mathrm{m}}$	Flow rate
N	Total number of flow field
r	Correlation coefficient
t_i	Time
U	Discrete velocity matrix in DMD analysis
U_{SJ}	Sweeping jet velocity
u	Velocity component along axial direction
u_i	Instantaneous velocity
$\tilde{u}_i(t)$	Phase-correlated contribution to the velocity
$\langle u_i(t) \rangle$	Phase-averaged velocity
$u'_i(t)$	Velocity fluctuating components
v_e	Entire signal of the different velocity
v_s	Segment of the entire signal of the different velocity
v	Velocity component along transverse direction
x	Axial coordinate

y	Transverse coordinate

Greek symbols

β	Phase angle of the sweeping jet oscillation in time domain
θ_{max}	Maximum deflection angle in space domain
λ	Eigenvalues of companion matrix C
ρ	Density of PIV tracking particles
$\Phi_n(\boldsymbol{x})$	DMD spatial mode
φ	Angle of the oscillator's diverging nozzle

Abbreviations

DMD	Dynamic mode decomposition
LIF	Laser-induced fluorescence
RMS	Root mean square
PIV	Particle image velocimetry
POD	Proper orthogonal decomposition
TR-PIV	Time-resolved particle image velocimetry

1. Introduction

Impinging jets, which can substantially improve heat transfer rates in the impact region, have been widely used for applications such as gas turbines, aircraft de-icing, and metallurgy (Han and Goldstein, 2001). However, their realization with a steady jet may not be efficient due to the limited region of influence centered on the impact region. In practice, a dense array of such jets is usually needed at the cost of a high flow rate. In this regard, the sweeping jet, which relies on a fluidic oscillator generating a temporally continuous but spatially oscillating jet in the transverse direction, can significantly extend the spatial extent of the impingement flow and improve the wall heat transfer. These effects have been confirmed by heat transfer measurements (Camci and Herr, 2002) and numerical studies (Thurman et al., 2016; Lundgreen et al., 2017). There is little doubt that the intensified wall heat transfer results primarily from spatiotemporal variation in the sweeping impinging jet flow, which differs fundamentally from a steady jet.

Quite a few efforts have been made to delineate the dynamics of sweeping jets issuing into an unbounded field. Inside the fluidic oscillator, due to the Coanda effect, the main jet is attracted to one sidewall in the interaction region of the fluidic oscillator. Near the jet exit, a small portion of the main jet stream returns through a feedback channel to the oscillator's inlet, causing the jet to detach and flip to the opposite side. Accordingly, the jet issued from the diverging nozzle exhibits a periodic sweeping motion in the transverse direction with a frequency up to 20 kHz (Gregory et al., 2013). Inside the fluidic oscillator, a phase-dependent analysis of flow patterns was undertaken using particle image velocimetry (PIV) measurements from Bobusch et al. (2013a) and Woszidlo et al. (2015), who identified a growing recirculation bubble between the main jet and attachment wall that was fed by the feedback flow and caused the main jet to oscillate. The internal interaction was also found to affect the external oscillation behaviors. Via surface-oil-flow visualization and hot-wire measurement, Koklu (2016) found that extending the jet exit substantially increased the jet deflection angle due to the Coanda effect between the jet and diverging exit wall. Similarly, Ostermann et al. (2015a) and Bobusch et al. (2013b) determined the influence of the oscillator's

divergence angle on the sweeping jet and claimed that a small divergence angle of the jet exit (φ = 90º) resulted in the attachment of the jet to the exit wall and thereby increased the jet's maximum deflection angle more than a larger divergence angle (φ = 125º). As for the sweeping impinging jet, measurements by Camci and Herr (2002) convincingly showed better heat transfer performance of a sweeping jet over a steady slot jet. Tesař (2009) determined a substantially higher total heat transfer rate in the sweeping impinging jet than in the steady jet, reaching an increase of 180% to 200% in some regimes. A recent numerical study of the sweeping impinging jet by Lundgreen et al. (2017) also determined an improvement in the heat transfer rate over the steady jet. An experimental study of Agricola et al. (2017) revealed that the impingement heat transfer of the sweeping jet is improved by an increase in Reynolds number. However, although a considerable increase in wall heat transfer is gained with the sweeping impinging jet (Camci and Herr, 2002; Tesař, 2009; Lundgreen et al., 2017), no experimental study has been conducted to elucidate the spatiotemporally varying flow behavior.

This study determines the unsteady behavior of a sweeping impinging jet. Experiments are carried out in a water tank using laser-induced fluorescence (LIF) visualization and planar time-resolved PIV (TR-PIV) measurement. The unsteady flow fields of six jet flow rates are investigated, corresponding to six Reynolds numbers (Re) between 2.7×10^3 and 9.3×10^3. The flow dynamics at two selected Reynolds numbers are discussed intensively in terms of phase-averaged velocity fields, vorticity fields, and velocity fluctuating components. Time-averaged velocity components and fluctuating components are also examined. Furthermore, the state-of-the-art dynamic mode decomposition (DMD) method is used to reveal energetic flow behavior at distinct frequencies. The phase correlation between the distinct flow patterns is finally determined by projecting the phase-averaged flow fields onto a reduced basis of DMD modes.

2. Experimental approaches

2.1 Test platform

The geometry of the fluidic oscillator explored in this study is shown in Fig. 1, which is commonly used in previous studies (Bobusch et al. 2013a; Woszidlo et al. 2015). The jet throat has a square cross section with a height (h) of 5 mm, resulting in a hydraulic diameter (d_h) of 5 mm. The depth of the oscillator is 5 mm, and the nozzle has a diverging angle (φ) of 90° and a length of 30 mm at the exit. The experiments are performed in a water tank as shown in Fig. 2. The fluidic oscillator is placed at center of the tank. The distance between the oscillator and the side walls of the tank is at least $80d_h$ (in both y and z directions) to avoid the side effect. Since the laser sheet is shot from top to bottom through the impingement plate, a rim is added to obstruct the water in order to avoid unstable liquid interface. Water is channeled from an overhead settling chamber and driven by gravity into the oscillator. A flowmeter monitors and controls the volume flow rate of the jet with an uncertainty level of 2.5%. By tuning the flowmeter, six supplied flow rates between 13.3×10^{-6} and 46.7×10^{-6} m^3/s are applied, as listed in Table 1. The jet velocity (U_{SJ}) is calculated based on the flow rate and the cross-section area of the oscillator throat. The corresponding Reynolds numbers based on the jet velocity and hydraulic diameter range from 2.7×10^3 to 9.3×10^3, well below the critical Reynolds number of 10×10^3, beyond which a fully developed turbulence state is achieved (Dimotakis, 2000). The spacing between the jet exit and impingement plate (L/d_h) is fixed at 8. The impingement flat plate is made of transparent plexiglass to allow the measurement laser sheet to pass through. The origin of the coordinate system is set at the center of the jet exit, with the x-axis pointing in the jet's axial direction and the y-axis pointing in the transverse direction (i.e., the direction of the jets' sweeping motion), as shown in Fig. 2.

2.2 LIF visualization

LIF is used to visualize the flow patterns induced by the sweeping impinging jet. As shown in Fig. 2, a 5-W, 532-nm-wavelength diode-pumped solid-state continuous-wave laser provides a laser sheet approximately 1 mm thick. A fluorescent dye, rhodamine-B, that was thoroughly premixed

with the jet supply water in the settling chamber is used to visualize and track the flow structures. A high-speed camera (Mikrotron, MC1362) with a 60-mm lens (Nikon) is used to capture the view of interest ($0 < x/d_h < 8$, $-16 < y/d_h < 16$) at 300 Hz. As shown in Fig. 2, LIF visualization is performed on the mid-span plane (x-y plane).

2.3 TR-PIV measurement

TR-PIV is used to measure the highly unsteady flow fields. The TR-PIV measurement has a setup similar to that of the LIF visualizations. Like the LIF visualization, TR-PIV measurement is performed on the same plane spanning in the transverse direction. The scaling pixel/mm is about 10 pixel/mm. To facilitate the PIV measurements, the entire water tunnel is seeded with glass beads ($\rho \approx 1050$ kg/m^3, $d \approx 10$ μm) as tracer particles. A high-speed camera (dimax HS4, pco.) operates at a dynamics sampling rate ranging between 1.5kHz to 3kHz depending on the Reynolds number. A multigrid cross-correlation technique (Raffel et al., 2013), in combination with subpixel recognition by Gaussian fitting (Yasuhiko et al., 2000), is applied with a final interrogation window size of 32 × 32 pixels with 50% overlap. In this time-resolved measurement, a measurement grid of velocity vectors with a spacing of 1.5 × 1.5 mm is then obtained. Due to the strong velocity gradient on the jet shear layer, more tracking particles are added to the settling chamber to ensure that there are at least 10 particles per interrogation window. As the major source of uncertainty, the root-mean-square fluctuation of the PIV-measured particle displacement is estimated to be about 0.08 pixel in the field images (Willert and Gharib, 1991). Therefore, the uncertainties in the measurements determined by recursive image interrogation are approximately 1% in the axial and transverse direction velocity components when the particle displacement is about 8 pixels in the interrogation window. To accelerate the computation process, the correlation scheme on the raw seeding pictures is based 1-2, 3-4, 5-6, etc. The sampling frequency of the flow vector field is at least two orders of magnitude higher than the examined oscillation frequency of sweeping jets, which is adequate to resolve the major frequencies in the unsteady flow fields. The total recording time is also dynamic to ensure at least 50 cycle periods are captured for each cases.

3. Data analysis

3.1 Phase-averaging method

The phase indicator is needed to reveal the phase-dependent variation of the sweeping impingement jet. Woszidlo et al. (2015) obtained the phase-averaged flow fields of internal and external fluidic oscillators based on time-resolved reference signals from pressure sensors. In our study, the sampling rate of the TR-PIV measurement is at least two orders of magnitude higher than the oscillation frequency of the sweeping jet, which provides adequate temporal resolution for phase identification. Therefore, the velocity information extracted from individual PIV snapshots is used for phase identification. As shown in Fig. 3, two specific locations in the flow field are selected to yield time-resolved values of difference between the transverse velocities (along *y* direction). These locations are in near-exit region and are symmetrical about the centerline of the jet exit to yield a signal (i.e., time-resolved values of velocity difference) with a high signal-to-noise ratio. Like the procedures used by Ostermann et al. (2015b) and Woszidlo et al. (2015), a numerical low-pass filter is imposed on the signal to reduce the noise while maintaining its phase and amplitude information, as shown in Fig. 4a. The entire signal is then correlated with a segment of the same signal to yield the correlation coefficient as

$$r(k) = \frac{1}{M}\sum_{m=1}^{M} v_s[m]v_e[m+k] \quad (1)$$

where v_e is the entire signal, v_s is the segment of the entire signal. *M* is the data size of v_s, and is approximately half of an oscillation period in length. Previous study revealed that the location of v_e has no significant influence on the result (Woszidlo et al. 2015). This yields an oscillating correlation coefficient where every other change of sign marks a full period, as shown in Fig. 4b. Based on the resulting oscillating correlation coefficient, a phase angle is assigned to each simultaneously recorded PIV snapshot. The size of the phase angle window for averaging is 3º for this study because it sufficiently reduces noise while maintaining the detailed flow features. As such, more than 150 instantaneous flow fields are used for phase averaging. The autocorrelation method does not provide a consistent starting point for all windows. Therefore, they are phase-

aligned based on the phase-averaged differential signal. In this study, the cycle begins when the jet is at the deflection position furthest to the left, that is, $\beta / \pi = 0$, as shown in Fig. 3. When the jet switches to the deflection position farthest to the right, $\beta / \pi = 1$. On the other hand, β / π changes from -1 to 0 when the jet switches from the right to the left side. The locations of the two reference sampling points vary at different flow rates due to the change in the maximum jet deflection angle θ_{max}. Please note that the β is defined in time, whereas θ is defined in space. The deflection angle of the jet θ in space may not change linearly with the time step β / π during the switching process, which will be investigated in the following section. The oscillation frequency is also calculated based on the differential velocity signal from the two reference positions.

3.2 DMD analysis

The DMD method separates a flow field into its mean value and higher modes that describe the fluctuations in the field. Unlike proper orthogonal decomposition (POD) analysis method, which extracts flow structures based on their energy ranking, DMD extracts flow structures based on their contributions to flow dynamics. By extracting spatial modes based on frequency content, DMD a suitable method to analyze dynamics of a flow system involving multiple frequency components like in the present study. Detailed information regarding the fundamentals and mathematical processes of the DMD algorithm was described by Schmid (2010; 2011). Examples for successful use of this method were presented by Liu and Zhang (2015), who identified and reconstructed the modes in a flow over a finite blunt plate, and Wen et al. (2015), who examined the dominant frequency distribution of synthetic jets in a separated flow. The mathematical description of DMD is only briefly introduced here.

In DMD, a time sequence of flow field data is organized by a matrix

$$U_1^N = \{\boldsymbol{u}_1, \boldsymbol{u}_2, \cdots, \boldsymbol{u}_N\} \tag{2}$$

where $\boldsymbol{u_i}$ is a vector representing a snapshot of the flow field at time t_i and N is the total number of tested flow fields. Consider another matrix U_2^{N+1}, The coefficients of the linear combination are stacked in a companion matrix C such that:

$$U_2^{N+1} = AU_1^N \approx U_1^N C \tag{3}$$

where the eigenvalues λ_i of C are approximations to some of the eigenvalues of a higher-dimension inter-snapshot linear map A. QR-decomposition of the data sequence U_1^N is used to calculate the companion matrix C. After the decomposition, the resulting dynamic modes can be expressed as:

$$\Phi_i = U_1^N v_i \tag{4}$$

where $\Phi_n(\boldsymbol{x})$ is the spatial basis mode function and v_i is the ith eigenvector of C. Although the long-time averaged flow field is kept in the velocity sequences, the corresponding DMD mode (Φ_0) is removed after the decomposition, in order to focus on the unsteady ones. The magnitude of the

dynamic mode Φ_i are defined as $||\Phi_i||$, and normalized by the norm of the full matrix Φ. The frequency of Φ_i is then defined as $f = \mathrm{Im}\{\log(\lambda_i)\}/2\pi\Delta t$.

In current study, the instantaneous flow field snapshots at least 50 sweeping cycles are used. Due to the computational limitation of the workstation, the sampling frequency of the flow field snapshot is reduced to 333Hz and 500Hz for the cases of $Re = 4.0 \times 10^3$ and 9.3×10^3, respectively. This sampling frequency is still two orders larger than the sweeping frequency at these two Reynolds numbers, respectively.

4. Results and discussion

Fig. 5 shows the overall performance of the oscillator, which plots the variation trend of the jet's maximum deflection angle θ_{max} and the jet's Strouhal number Sh against the Reynolds number. The maximum deflection angle is obtained from the u and v components of the highest velocity magnitudes in the near-exit region from the long-time averaged flow field. As shown in Fig. 5a, the maximum deflection angle increases with the Reynolds number and reaches a saturation value of about θ_{max} = 81º at $Re = 6.7 \times 10^3$ due to the constraint of the oscillator geometry. Previous studies have revealed that sweeping frequency f almost increases linearly with the supply flowrate (Tesař et al. 2013). By defining the Strouhal number Sh as

$$\mathrm{Sh} = \frac{f d_h}{U_{SJ}} \tag{5}$$

, previous studies found that Sh is almost a constant value regardless of the Re. In current study, Fig. 5b illustrates that Strouhal number Sh is almost a constant value, especially after $Re = 5.3 \times 10^3$. As the Reynolds number increases from lower value, Sh decreases a little. As revealed by Bobusch et al. (2013 a) and Woszidlo et al. (2015), a separation bubble inside the oscillator between the main jet and the wall of the interaction region is responsible for pushing the jet to the opposite side and causing the external jet deflection. From current observations, the change in the Reynolds number is expected to affect the flow interaction inside the fluidic oscillator to some extent, which results in the changing of the maximum deflection angle as well as the Strouhal number Sh.

The unsteady behavior in the near-exit region is believed to have a direct effect on the impingement behavior. Two Reynolds numbers are selected (i.e., $Re = 4.0 \times 10^3$ and 9.3×10^3), with moderate and saturated deflection angles, respectively. At the lower Reynolds number $Re = 4.0 \times 10^3$, the jet sweeping motion is apparent with a moderate deflection angle θ_{max} = 40º without attaching to the diverging exit wall. At the higher Reynolds number $Re = 9.3 \times 10^3$, the jet maximum deflection angle is in a saturated state with a value θ_{max} = 83º, and the jet can fully attach to the diverging exit wall. The time-resolved jet deflection angle θ_{jet}, the jet peak velocity U_{max}, the jet

width, and the jet mass flow rate are obtained from phase-averaged flow fields with a phase interval of $\pi/18$. Because of the jet's considerable lateral extent, an appropriate comparison of the jet's properties must be performed at a fixed distance from the jet throat. Therefore, a polar coordinate system is adopted. As shown in Fig. 3, the jet deflection angle and jet properties are obtained along an arc with a distance of $5.5d_h$ from the jet throat, that is, $3d_h$ to the center of the jet exit along the centerline. The jet width is the normal width of the local velocity profile with $U \geq 50\% U_{max}$. The mass flow rate is calculated based on the jet width and the spatially averaged velocity. Based on the spatial resolution and velocity uncertainty in current PIV measurement, the uncertainty of the jet width and mass flow rate are about 12% according to the mean values. Fig. 6a plots the time-resolved jet deflection angle θ_{jet} at $Re = 4.0 \times 10^3$. The temporal variation of the jet deflection angle indicates that the sweeping motion appears sinusoidal. Fig. 6b plots the jet peak velocity, jet width, and jet mass flow rate oscillating around their corresponding mean values. The RMS values are about 0.07, 0.12 and 0.07, respectively. The instantaneous jet properties show no remarkable trend with the variation in jet deflections. Two weak peaks along the plot of the jet width are captured at around $\beta / \pi = \pm 1/2$, which correspond to the zero-deflection angle. At $Re = 9.3 \times 10^3$, as shown in Fig. 7a, the time-resolved jet deflection angle does not follow the corresponding sine wave as well as that at $Re = 4.0 \times 10^3$. The jet experiences a rapid switching process from one side of the exit to the other, which is indicated by the steep slope of the change in the jet deflection angle around $\beta / \pi = \pm 1/2$. In contrast, the jet appears to remain on the maximum deflection angles for a longer period with an expected slower motion at around $\beta / \pi = 0$ and ± 1. This is believed to be caused by the Coanda effect between the jet and the diverging exit wall. When the jet is at the maximum deflection position, the jet is attaching to the diverging exit wall. The Coanda effect forces the jet to stay at this position for a longer time. This effect was also used to increase the jet maximum deflection angle in previous study (Koklu 2016). Accordingly, the instantaneous jet peak velocity, jet width, and jet mass flow rate at different deflection angles oscillate more significantly, as shown in Fig. 7b. The RMS values are about 0.17, 0.23 and 0.09, respectively. The maximum jet width corresponds to the zero-deflection angle at around $\beta / \pi = \pm 1/2$. In addition, it is accompanied by the highest mass flow rate and the lowest jet peak velocity. The opposite is true for the maximum

of the jet deflection angle at around $\beta / \pi = 0$ and ± 1, which is accompanied by the highest jet peak velocity. According to Woszidlo et al. (2015), the variation in the jet properties may be due to the internal dynamics of the fluidic oscillator, that is, the change in the blocking effect of the separation bubble and the jet impingement on the internal wall. From the current observations, the diverging exit wall may also contribute to the oscillation of the jet properties. Under the combined effect, the jet in the near-exit region remains on the maximum deflection angle for a longer time with more concentrated jet momentum.

4.1 LIF Visualization

Figs. 8 and 9 present sequences of snapshots to show the sweeping motion of the jets at the two selected Reynolds numbers from the qualitative LIF visualizations. The correlation between the flow behavior in the near-exit region and the near-wall impact region are focused. Since the flow field is generally symmetrical to the centerline, the oscillating flow during one half cycle at four phase angles (i.e., $\beta / \pi = -1/9$, 2/9, 5/9, and 8/9) are selected. During this half cycle, the jet sweeps from the left side to the right side of the flow field. At the lower Reynolds number $Re = 4.0 \times 10^3$ as shown in Fig. 8, the jet sweeps with a moderate deflection angle in the near-exit region. Accordingly, the impact region on the wall also oscillates from the middle of the near-wall region to the left outer side. Therefore, the sweeping impinging jet can cover a large region of influence on the wall in a time-averaged sense. In addition, two interesting observations can be made. Due to the curved jet column during the sweeping motion, a phase difference exists between the fluid motions in the near-exit and impact regions. At a phase angle $\beta / \pi = 8/9$ as shown in Fig. 8d, the jet in the near-wall region sweeps to the right side, whereas the jet in the impact region remains on the left side. In addition, the flow in the impact region remains on the outer side for a long time. For example, from phase angles $\beta / \pi = 2/9$ to 8/9, a persistent flow on the left outer side is found in the impact region, which will dissipate in the following half cycle. Due to the impermeability constraint of the impingement plate, the persisting impinging flow generates a wall-jet flow at $\beta / \pi = 5/9$, as shown in Fig. 8c, which is commonly found in a steady impinging jet (Hadžiabdić and Hanjalić, 2008). Due to the symmetry of the flow field, another wall-jet flow will form on the right side of the flow field in the following one half cycle.

At the higher Reynolds number $Re = 9.3 \times 10^3$, the sweeping jet's maximum deflection angle reaches its saturation status, as shown in Fig. 9. Consistent with that revealed in Fig. 7a, the switching process of the jet from one side to the other is more intense. A sharp turning corner in the jet column is captured during the switching process, which resulting in a more significant phase difference between the jet flow in near-exit region and in near-wall region than that at $Re = 4.0 \times$

10^3. As shown in Fig. 9c, the turning corner can occur near the jet exit, at about $3d_h$. From the time-resolved deflection angle as revealed in Fig. 7a and the corresponding velocity field measured by PIV, the tangential velocity caused by the transverse sweeping motion around the turning corner is calculated to be close the local jet velocity along the jet column. At locations farther from the jet exit, the tangential velocity will surpass the jet velocity, resulting in a sharp turning corner. This sharp turning corner causes the jet column to "break" in the near-exit region before it impinges on the wall. Therefore, the impact region around the middle of the near-wall region is not captured. LIF visualization also confirms that the jet can attach to both sides of the diverging exit wall. Due to the Coanda effect, the jet remains on the most deflected angle for a longer time in the near-exit region.

4.2 PIV measurements

In Figs. 10 and 13, half oscillation periods at Reynolds numbers $Re = 4.0 \times 10^3$ and 9.3×10^3 are presented at four selected phase angles $\beta / \pi = -1/9$, 2/9, 5/9, and 8/9. The contours of axial (x-axis direction) and transverse (y-axis direction) velocity components are presented. The flow fields are normalized by the sweeping jet velocity U_{SJ}. Respective uniform velocity vectors are added to enhance the visibility of the dynamics. In addition, it has been well documented that the edge shear layer surrounding the jet is one of the main processes that influence a jet's dynamics and heat transfer (Hadžiabdić and Hanjalić, 2008). Therefore, the vorticity field is also plotted to show the interaction between the jet shear layer and the impingement wall. Velocity fluctuating components along the axial and transverse directions are also plotted to show the distribution of jet turbulence, as calculated from phase-averaged flow fields. The investigated flow field consists of a turbulent jet with a highly periodic sweeping motion. Hence this periodic motion can be seen as an organized wave in a turbulent shear flow (Greco et al. 2016). For this reason, the phase-averaged velocity fluctuating components are calculated through the application of the triple decomposition (Hussain and Reynolds, 1970; Kitsios et al., 2010):

$$\mathrm{u}_i(t) = U + \tilde{u}_i(t) + u'_i(t) \tag{6}$$

where U is the time-averaged velocity component, $\tilde{u}_i$ is the phase-correlated contribution to the velocity and u'_i is the velocity fluctuating components.

The phase-averaged velocity is

$$\langle u_i(t) \rangle = \lim_{N \to \infty} \frac{1}{N} \sum_{n=0}^{N-1} u_i(t + n\tau) \tag{7}$$

where N is the number of the instantaneous flow fields at same phase and n is a natural number. The phase-correlated organized contribution to velocity is

$$\tilde{u}_i(\mathrm{t}) = \langle u_i(t) \rangle - \mathrm{U} \tag{8}$$

and the fluctuating components are evaluated as

$$u'_i(\mathrm{t}) = \mathrm{u}_i(t) - \langle u_i(t) \rangle \tag{9}$$

The PIV-measured flow quantities in a half oscillation period at $Re = 4.0 \times 10^3$ are presented in Fig. 10. Fig. 10a plots the phase-averaged flow field at phase angle $\beta / \pi = -1/9$. Like that revealed by LIF visualization, the jet column is curved during the sweeping process. The contour of the axial velocity and velocity vectors show that the jet in the near-exit region approaches its left-most position, whereas the jet flow in the near-wall impact region is at the middle of the near-wall region. The plot of transverse velocity shows that two wall-jet flows are formed outboard of the near-wall region. Because the jet flow simply switches back from the right side, the outboard wall-jet flow on the left side is believed to be induced in the previous cycle. In order to reveal the impinging process, phase-averaged velocity magnitude profiles along four transvers lines at different distance from the impingement plate are extracted. As shown in Fig. 11, the jet velocity decreases generally when the jet is approaching to the wall at the locations far from the impingement plate ($2.31d_h \sim 1d_h$). At the location close to the wall ($0.33d_h$), the impingement plate presence causes an adverse pressure gradient leading to an abrupt velocity decrease (O'Donovan, 2005; Greco et al., 2016). As such, a plateau around the impact region ($y \approx -2d_h$) is formed along the velocity profile. In addition, another peak is induced on the right side of the flow field ($y \approx 9d_h$). As shown by the velocity vectors in Fig. 10a, the impinging flow on the near-wall region deflect more on transverse direction when it meets the impinging plate and forms the wall-jet flow. Strong local vorticity and velocity fluctuating components are found not only around the impact region but also at the deflection region of the flow where the wall-jet flow starts. The plots of the axial and transverse velocity fluctuating components also confirm the moderate jet turbulence, which can be up to 15% of the jet velocity.

At a phase angle $\beta / \pi = 2/9$ (Fig. 10b), the jet in the near-exit region begins to sweep to the right side of the flow field, as shown by the plot of axial velocity. In contrast, the impact region oscillates to the left outboard location around $y / d_h = -3$. The transverse velocity in the impact region increases in strength compared with the axial velocity due to the jet's deflected angle, which deflects the jet's momentum more in the transverse direction. Steady jets have a common problem of the location of the jet shear layer where high turbulence is located. The jet shear layer usually

bends and diverges before reaching the surface, and this divergence carries the flow turbulence away from the impingement surface, at least from the impact region around the stagnation point (Tesař, 2015). The plot of the vorticity contour shows that the windward shear layer of the current sweeping jet impinges directly on the wall due to the curved jet column during the switching process, which can enhance the turbulence in the impact region. In the plots of velocity fluctuating components, an obvious mismatch can be seen between the locations of the axial and transverse velocity fluctuating components. Strong axial velocity fluctuating components are found in the near-exit region and on the right side of the jet column; in contrast, strong transverse velocity fluctuating components are found approaching the wall and on the left side of the jet column. These findings are consistent with the velocity distributions in the near-exit and near-wall regions.

At phase angle $\beta / \pi = 5/9$ (Fig. 10c), the jet in the near-exit region is sweeping to a deflection position of almost zero. The jet in the near-wall region remains on the left side of the flow field, resulting in persistent impingement. Therefore, the different distribution of the velocity components between the near-exit and near-wall regions is more significant. During the switching process, the plot of vorticity shows that the windward jet shear layer experiences significant stretching. The jet shear layer is shed from the jet column and attaches to the wall. The distribution of velocity fluctuating components is consistent with that of the velocities. Much greater velocity fluctuation in the axial direction is induced in the near-exit region, whereas its counterpart is mostly in the impact region on the left side. At $\beta / \pi = 8/9$ (Fig. 10d), the jet in the near-exit region arrives at its right-most right-side position. The flow patterns are similar to $\beta / \pi = -1/9$ mirrored at the centerline of the flow field. By plotting the flow fields at $\beta / \pi = -1/9$ and 8/9 together, this symmetry is more obvious, as shown in Fig. 12. The impact region then begins to oscillate to the right side of the near-wall region.

The PIV-measured flow quantities in a half oscillation period at $Re = 9.3 \times 10^3$ are presented in Fig. 13. At a phase angle $\beta / \pi = -1/9$, the jet in the near-exit region is at the left-most deflection position. However, the flow at the impact region on the right side remains strong, as shown by the

plots of the axial and transverse velocities. Due to the increased jet deflection angle, the distance between the impact regions on both outboard sides also increases. A near-wall vortex is induced at the deflection region of the impinging flow on the furthest outboard right side (circle indicated by arrow). Correspondingly, strong local vorticity and velocity fluctuating components are also induced between the near-wall vortex and impingement plate. In addition, an entrainment flow is observed very close to the exit, as shown by the velocity vectors in the plot of axial velocity. As revealed by Bobusch et al. (2013a), a vortex can form in the diverging nozzle at the inactive region, entraining fluid from outside the flow field.

At a phase angle $\beta / \pi = 2/9$, the impinging flow on the right side dissipates rapidly, as shown by the plot of transverse velocity. The jet in the near-exit region begins to sweep to the right side of the flow field, whereas the jet flow in the near-wall region remains at its left-most position. Due to the rapid and intense switching process, as revealed by the change in the time-resolved jet deflection angle (Fig. 7a), the main jet column begins to break, as indicated by the lower-velocity region near the exit, as shown in the plot of axial velocity. At a phase angle $\beta / \pi = 5/9$, the jet column breaks with a sharp turning corner in the near-exit region at around $x / d_h = 3$, which is shown clearly by the plot of transverse velocity. The jet in the near-exit region is passing through the centerline of the flow field, whereas a large region of the jet flow with a strong transverse velocity is left behind on the left side. As the flow impinges on the wall, a new strong near-wall vortex (circle indicated by an arrow) is formed on the left side. At a phase angle $\beta / \pi = 8/9$, the jet in the near-exit region approaches its right-most position. The flow patterns are similar to those of $\beta / \pi = -1/9$ mirrored at the centerline of the oscillator. A strong impinging flow begins to form on the right side of the near-wall region.

In Fig. 14, profiles of jet speed along the centerline ($y = 0$) of the flow fields at the two selected Reynolds numbers are presented. In general, the sweeping jets suffer a more significant decay than a continuous steady jet does (Ghasemi et al. 2015). This is partly due to the jet sweeping motion which causes a larger influencing area, and partly due to the relatively high turbulent level of the

jet flow. Since the jet has a larger spreading angle at the higher Reynolds number, the jet flow decays more significantly, which could limit its impinging effect, especially in the middle of the near-wall region. It is worth noting that, in current coordination system, there is still a distance of about $2.5d_h$ from the origin point ($x = 0$ in Fig. 14) to the jet throat. The distributions of the time-averaged velocity components and fluctuating components in transverse direction in the near-exit region and near-wall region at $Re = 4.0 \times 10^3$ and 9.3×10^3 are shown in Fig. 15. At $Re = 4.0 \times 10^3$ in the near-exit region ($x = 3.4d_h$), the axial velocity component shows a local minimum at the centerline (around $y = 0$) and a maximum near $y/d_h \approx -1.4$ (also $y/d_h \approx 1.4$ on the other side of the flow field, not shown here) as shown in Fig. 15a. The location of the peak value is closely related to the half-maximum jet deflection angle ($\theta_{max}/2 = 20^o$) and distance from the exit ($x = 3.4d_h$). The double-peak profile shows that the sweeping motion of the jet can cause uneven distribution of the jet momentum. The axial velocity component in the near-wall region ($x = 7.7d_h$) also shows double-peak profile. At the higher Reynolds number $Re = 9.3 \times 10^3$, the axial velocity in the near-exit region has a peak located at a further outboard location near $y/d_h = 3.5$ due to the large maximum deflection angle. The peak value of the axial velocity, however, becomes smaller. This is partly because the jet dissipates more significantly with a larger deflection angle (or spreading area), and partly become the flow is more directed to transverse direction. In the near-wall region, the influenced area becomes larger due to the larger deflection angle of the sweeping jet. However, the axial velocity around the middle of the near-wall region is even lower than that at $Re = 4.0 \times 10^3$, indicating the remarkably uneven spatial distribution of the impingement effect. As discussed above, this uneven distribution is caused by the longer residence time of the jet on the maximum deflection angle and the breaking up of the jet column.

The profiles of transverse velocities at these two Reynolds numbers are generally similar to those of the axial velocities; however, close examination of Fig. 15a still reveals the different features. First, the transverse velocity increases more significantly with the Reynolds number since the larger deflection angle turns the jet momentum more in the transverse direction. Second, a small region of opposite transverse velocity (indicated by the black arrow) is found at the edge of the

sweeping-jet flow field. As shown in the phase-averaged flow field (Fig. 10), the surrounding fluid is attracted to the jet column due to the pressure gradient caused by the high-speed jet flow. In addition, a local peak can be seen at the most outboard locations (indicated by the red arrow) in the near-wall region at $Re = 9.3 \times 10^3$, which is believed to be caused by the near-wall vortex induced by the strong impinging flow outboard of the near-wall region. This near-wall vortex can strengthen the transverse velocity near the wall by its favorable rotation direction. As shown in Fig. 15b, distributions of the velocity fluctuating components are similar to those of the velocities. At the higher Reynolds number, in addition to the major double peaks of velocity fluctuation in the near-wall region, local peaks of high fluctuation are also induced by the near-wall vortex at the most outboard locations in not only the transverse but also the axial directions.

4.3 DMD analysis

As revealed in the phase-averaged flow fields, the motions of the sweeping impinging jet differ significantly at different regions. A previous study (Bobusch et al., 2013a) also revealed that the internal flow field of a sweeping jet consisted of superharmonic oscillations. To further reveal the complicated dynamics, DMD analysis is applied to the time-resolved PIV snapshots at two Reynolds numbers $Re = 4.0 \times 10^3$ and 9.3×10^3.

At $Re = 4.0 \times 10^3$, the DMD analysis shows that the dominant flow patterns occur at the maximum deflection angle. As shown in Fig. 16a, all eigenvalues of the DMD spectra in this highly periodic flow lies on a unit circle (Mezic et al 2005; Rowley et al. 2009). As shown in Fig. 16b, mode 1 captures the jet-oscillation frequency with much higher energy than the others. The corresponding fluctuating flows are located on the two outer sides of the flow field, as shown in Fig. 16c. The flow behaviors captured by the real part of mode 1 correspond to the most deflected flows in the near-exit region, whereas the imaginary part corresponds to the outboard flows in the near-wall region. Previous study revealed that both real parts and the imaginary parts of the DMD mode contribute to the description of flow dynamics (Muld et al. 2012). In current study, the phase difference between the real and imaginary parts describes the convection process of the jet from the near-exit region to the near-wall region. With lower energy, mode 2 captures flow along the centerline of the flow field, as shown in Fig. 16d. Such flow patterns have a frequency twice that of the jet-oscillation frequency due to the definition of one oscillation period, which corresponds to the time during which the sweeping jet switches from one side to the other and back. During this period, the jet passes the center line of the flow field twice. Similarly, the real part of mode 2 largely captures the flow in the near-exit region and the imaginary part for the near-wall region.

To examine the phase correlation between these major flow patterns, phase-averaged flow fields with a phase interval of $\pi/18$ are projected onto the two most energetic modes. The corresponding phase coefficient is obtained by

$$\alpha_i^n = U^n \cdot \Phi_i / ||\Phi_i|| \quad (10)$$

where *n* is the *n*th of phase-averaged flow fields and *i* is the *i*th of DMD modes. The corresponding phase coefficients of the mode real parts are plotted in Fig. 17. Because these distinct flow patterns captured by modes 1 and 2 occur at different phase angles, one coefficient wanes while the other waxes. The flow captured by the real part is about $\pi/4$ earlier than that captured by the imaginary part (not shown here). This corresponds to the advection of the flow from the near-exit region to the near-wall region (Liu et al., 2014).

By plotting the temporal variations of the DMD modes, the phase correlations between the most energetic flow patterns can be presented more intuitively. As indicated by the dashed lines in Fig. 17, three phase angles (β / π = 0, 1/2, and 1) are selected. The flow patterns captured by each DMD mode at different phase of the sweeping cycle are obtained by adding the real and imaginary parts of the mode and weighted by the phase coefficients, which is an inverse operation of Eq. 10. At β / π = 0, the jet is arriving at the left-most position in the phase-averaged flow field, as shown in Fig. 18a. The coefficient of real part of mode 1 is near the positive peak value (Fig. 17). Therefore, a strong flow is captured by mode 1, with the positive axial velocity on the left side of the flow field, as shown in Fig. 18b. In contrast, the coefficient of the real part of mode 2 is near zero. Because a phase delay occurs between the coefficients of the real and imaginary parts of mode 2, the weak flows captured by mode 2 are resulted mostly from the imaginary part with a positive axial velocity in the near-wall region, as shown in Fig. 18c. Note that DMD mode 0 captures a time-averaged flow field with positive axial velocity. The addition of the fluctuation modes with the time-averaged mode can result in strong jet flow on the left side of the flow field and weak flow around the middle of the near-wall region. At a phase angle β / π =1/2, the jet in the near-exit region is at the zero-deflection position in the phase-averaged flow field, whereas the jet in the near-wall region remains on the left side of the flow field. Therefore, the flows captured by the real part of mode 1 are relatively weak because the corresponding coefficient is near zero. The weak flows captured by mode 1 are mostly due to the imaginary part and contribute to the flows in the near-wall region. In contrast, the flows captured by the real part of mode 2 strengthen because the

coefficient is at its positive peak. A strong flow with positive axial velocity around the centerline is added to the jet flow in the near-exit region. At the end of this half oscillation cycle $\beta / \pi = 1$, the jet arrives at the right-most position. Accordingly, the flows captured by mode 1 are near those at $\beta / \pi = 0$ mirrored at the centerline of the flow field, indicating the completion of the half oscillation cycle. For mode 2, the captured flows become similar to those at $\beta / \pi = 0$, indicating the completion of an entire oscillation cycle.

At $Re = 9.3 \times 10^3$, as shown in Fig. 19, the energy spectrum is similar to that at $Re = 4.0 \times 10^3$, but with higher frequencies. It can be seen that mode 3 has a frequency near that of mode 2, whereas its frequency is near that of mode 1 at $Re = 4.0 \times 10^3$. Because the current sampling frequency is much higher than the oscillation frequency (at least two orders higher), DMD analysis can resolve even a minor frequency difference between the modes. The flow patterns captured by mode 3 are very similar to those captured by mode 2, but with a minor difference in frequency. Unlike that at $Re = 4.0 \times 10^3$, captured by the imaginary part of mode 1, the flow at the impact region is stronger and coupled with the near-exit flow on the other side of the flow field, as shown in Fig. 19c, because the impinging flow is more persistent in the outboard impact region, as shown in the phase-averaged flow fields (Fig. 13). As such, the flow at the impact region and the near-exit flow on the same side have a phase difference of π. In addition, the flow with superharmonic jet-oscillation frequencies in mode 2 is only captured in the near-exit region, but not in the near-wall region, due to the weak flow, as shown in Fig. 19d. This finding confirms that the spatial distribution of the energetic flow patterns is remarkably uneven in the near-wall region at the higher Reynolds number. This is closely related to the uneven sweeping motion and the breaking of the jet column in the near-exit region, as discussed above. It is interesting to see that the flow with a superharmonic jet-oscillation frequency in mode 2 is bound to $x/d_h \approx 3$, which coincides with the location of the sharp turning corner where the jet column breaks (Fig. 13c). Within this bounded near-exit region, the energetic flow patterns are more evenly distributed than those in near-wall region.

Phase correlations of the real parts of the first two DMD modes are presented in Fig. 20. Because the real parts of the modes capture the flows in the near-wall region, they are about $\pi/4$ later than the imaginary parts. Unlike that at $Re = 4.0 \times 10^3$, the coefficients of mode 2 have relatively large negative values. Together with the flow captured by mode 2, they can result in a flow with negative axial velocity in the near-exit region. The temporal variations of the two DMD modes at the three phase angles (as shown in Fig. 20) are presented in Figure 21. At $\beta / \pi = 0$, as shown in Fig. 21a, the jet is at the left-most position in the phase-averaged flow field. Therefore, mode 1 captures a strong deflected jet flow with positive axial velocity on the left, as shown in Fig. 21b. In mode 2, as shown in Fig. 21c, a flow with negative axial velocity is captured in the near-exit region because the corresponding phase coefficient is at its negative peak. Such flow contributes to the entrainment flow near the exit in the phase-averaged flow field. At $\beta / \pi = 1/2$, the jet in the near-exit region is at the zero-deflection position; it breaks up and leaves a strong impinging flow in the near-wall region on the left side of the phase-averaged flow field. Therefore, the flow captured by the real part of mode 1 is weak, whereas the imaginary part contributes a near-wall flow on the left of the flow field. In mode 2, a flow with strong positive axial velocity is captured in the near-exit region around the centerline of the flow field, contributing to the jet flow in the near-exit region in the phase-averaged flow field. At $\beta / \pi = 1$, the jet arrives at its right-most position. As mode 1 completes a half oscillation cycle, mode 2 varies for an entire oscillation cycle.

5. Conclusions

In this study, the unsteady behavior of a sweeping impinging jet at $L/d_h = 8$ is experimentally investigated with TR-PIV. With an increase in the Reynolds number from 2.7×10^3 to 9.3×10^3, the results show an approximately linear increase in the sweeping frequency, especially at the higher Reynolds numbers. The saturation of the sweeping jet is reached at $Re = 6.7 \times 10^3$. The unsteady flow behavior of the sweeping impinging jet at two selected Reynolds numbers $Re = 4.0 \times 10^3$ and 9.3×10^3 is then examined with the phase-averaged flow fields. State-of-the-art DMD analysis is conducted to capture the energetic events superimposed in the unsteady flow.

The unsteady behavior in the near-exit region is compared by examining the time-resolved jet deflection angle, the instantaneous jet width, and the peak velocity. At $Re = 4.0 \times 10^3$, the sweeping motions in the near-exit region are more evenly distributed, and the jet width and peak velocity are relatively constant. At the higher Reynolds number $Re = 9.3 \times 10^3$, the jet in the near-exit region shows more uneven sweeping motions. The jet remains at the maximum deflection angle for a longer time during one oscillation cycle with a narrower jet and a higher peak velocity, resulting in a faster switching process.

At $Re = 4.0 \times 10^3$, due to the oscillation motion of the impact region along the wall, the sweeping impinging jet exerts a large region of influence. The flow in the impact region is found to remain on the outer sides of the near-wall region for a long time, generating a wall-jet flow. Therefore, by plotting the time-averaged velocity components and velocity fluctuating components near the wall, the profiles of the impingement effect show a double peak on both outer sides and a minimum in the middle of the near-wall region.

At $Re = 9.3 \times 10^3$, due to the rapid and intensive sweeping process, the jet column breaks in the near-wall region. This, together with the uneven sweeping motions of the sweeping jet in the near-exit region, results in a strong impinging flow on both outer sides but a weak flow in the middle of the near-wall region. A near-wall vortex is also induced by the strong impinging flow. The profiles of the time-averaged velocity components and fluctuating components have a higher double-peak value but an even lower minimum value at the middle of the near-wall region than those at the

lower Reynolds number. In addition, the local peaks of the impingement effect at most outboard sides of the near-wall region are also induced by the near-wall vortex.

The DMD analysis of the jet flow at $Re = 4.0 \times 10^3$ demonstrates that the dominant first DMD mode featured by the jet-oscillation frequency corresponds to the most deflected flows. The second mode with twice the jet-oscillation frequency mostly captures the flows passing through the centerline of the flow field. At $Re = 9.3 \times 10^3$, the first DMD mode shows that the impinging flow is stronger and remains in the impact region for a longer time. Therefore, the impinging flow at the impact region and the jet in the near-exit region on the same side of the flow field has a phase difference of π. The spatial distribution of the most energetic flow behavior is remarkably uneven in the near-wall region. Bounded by the location where the jet column breaks, the energetic flow patterns in the near-exit region are more evenly distributed.

As a result of this investigation, a better understanding of the unsteady behavior of sweeping impinging jets is achieved, and it should be helpful for future applications and optimizations of sweeping impinging jets in heat transfer. For example, in order to provide a more even distribution of the impingement, the jet-to-exit distance can be optimized based on current findings. In addition, using multiple sweeping jets is another option. But the oscillation phase between the neighbor sweeping jets should be synchronized in order to better apply array of them. The synchronization problem will be investigated in further work.

Acknowledgments

The authors gratefully acknowledge the financial support from the National Natural Science Foundation of China (Grant nos. 11702172 and 11725209) for this study.

References

1. Agricola, L., Hossain, M. A., Prenter, R., Lundgreen, R., Ameri, A., Gregory, J., and Bons, J.P., "Impinging Sweeping Jet Heat Transfer," AIAA paper, 2017, 2017-4974.
2. Bobusch, B.C., Woszidlo, R., Bergada, J.M., Nayeri, C.N.N., and Paschereit, C.O., "Experimental study of the internal flow structures inside a fluidic oscillator," Experiments in Fluids, 2013a, 54 (6): p.1559.
3. Bobusch, B.C., Woszidlo, R., Krüger, O., and Paschereit, C.O., "Numerical investigations on geometric parameters affecting the oscillation properties of a fluidic oscillator," AIAA paper, Computational Fluid Dynamics Conference, 2013b, 2013-2709.
4. Camci, C., and Herr, F., "Forced convection heat transfer enhancement using a self-oscillating impinging planar jet," Journal of Heat Transfer, 2002, 124(4), p.770-782.
5. Dimotakis, P.E., "The mixing transition in turbulent flows," Journal of Fluid Mechanics, 2000, 409: p.69-98.
6. Ghadi, S., Esmailpour, K., Hosseinalipour, S. M., and Mujumdar, A., "Experimental study of formation and development of coherent vortical structures in pulsed turbulent impinging jet," Experimental Thermal & Fluid Science, 2016, 74: p.382-389.
7. Ghasemi, A., Roussinova, V., Balachandar, R., and Barron, R. M., "Reynolds number effects in the near-field of a turbulent square jet," Experimental Thermal & Fluid Science, 2015, 61, p.249-258.
8. Greco, C.S., Castrillo, G., Crispo, C.M., Astarita, T., and Cardone, G., "Investigation of impinging single and twin circular synthetic jets flow field," Experimental Thermal & Fluid Science, 2016, 74: p.354-367.
9. Gregory, J., and Tomac, M.N., "A review of fluidic oscillator development," AIAA paper, Fluid Dynamics Conference, 2013-2474.
10. Hadžiabdić, M., and Hanjalić, K., "Vortical structures and heat transfer in a round impinging jet," Journal of Fluid Mechanics, 2008, 596: p.221-260.
11. Han, B., and Goldstein, R., "Jet-impingement heat transfer in gas turbine systems," Annals of the New York Academy of Sciences, 2001, 934(1): p.147-161.
12. Hussain, A.K.M.F., Reynolds, W.C., "The mechanics of an organized wave in turbulent shear flow," Journal of Fluid Mechanics, 41 (02) (1970) 241–258.
13. Kitsios, V., Cordier, L., Bonnet, J.P., Ooi, A., Soria, J., "Development of a nonlinear eddy-viscosity closure for the triple-decomposition stability analysis of a turbulent channel," Journal of Fluid Mechanics, 664 (2010) 74–107.
14. Koklu, M., "Effect of a Coanda extension on the performance of a sweeping-jet actuator," AIAA Journal, 2016, 54(3): p.1-4.
15. Liu, Y.Z., Shi, L.L., and Yu, J., "TR-PIV measurement of the wake behind a grooved cylinder at low Reynolds number," Journal of Fluids and Structures, 2011, 27(3): p.394-407.
16. Liu, Y., and Zhang, Q., "Dynamic mode decomposition of separated flow over a finite blunt plate: time-resolved particle image velocimetry measurements," Experiments in Fluids, 2015, 56(7).

17. Liu, Y., Zhang, Q., and Wang, S., The identification of coherent structures using proper orthogonal decomposition and dynamic mode decomposition. Journal of Fluids & Structures, 2014, 49(8): p.53-72.
18. Lundgreen, R.K, Hossain, A.F., Prenter, R., Bons, J. P., Gregory, J.W., and Ameri, A., "Impingement heat transfer characteric of a sweeping jet," AIAA paper, Aerospace Sciences Meeting, 2017-1535.
19. Mezic´, I. "Spectral properties of dynamical systems, model reduction and decompositions." Nonlinear Dynamics. 2005, 41, 309–325.
20. Muld, T. W., Efraimsson, G., & Dan, S. H., "Flow structures around a high-speed train extracted using proper orthogonal decomposition and dynamic mode decomposition," Computers & Fluids, 2012, 57(4), 87-97.
21. O'Donovan, T.S., "Fluid flow and heat transfer of an impinging air jet," Ph.D. thesis, Department of Mechanical & Manufacturing Engineering, Trinity College Dublin, 2005.
22. Ostermann, F., Woszidlo, R., Nayeri, C.N., and Paschereit, C.O., "Experimental comparison between the flow field of two common fluidic oscillator designs," AIAA paper, Aerospace Sciences Meeting, 2015a, 2015-0781.
23. Ostermann, F., Woszidlo, R., Gaertlein, S., Nayeri, C.N., and Paschereit, C.O., "Phase-averaging methods for the natural flow field of a fluidic oscillator," AIAA Journal, 2015b, 53(8): p.2359-2368.
24. Raffel, M., Willert, C.E., and Kompenhans, J., "Particle Image Velocimetry: A Practical Guide," 2013, Berlin: Springer.
25. Rowley, C. W., Mezic, I., Bagheri, S., Schlatter, P. & Henningson, D. S. "Spectral analysis of nonlinear flows." Journal of Fluid Mechanics, 2006, 641, 115–127.
26. Schmid P.J., "Dynamic mode decomposition of numerical and experimental data," Journal of Fluid Mechanics, 2010, 656 (10), p.5-28.
27. Schmid, P.J., "Application of the dynamic mode decomposition to experimental data," Experiments in Fluids, 2011, 50(4): p.1123-1130.
28. Tesař, V., "Enhancing impinging jet heat or mass transfer by fluidically generated flow pulsation," Chemical Engineering Research & Design, 2009, 87(2): p.181-192.
29. Tesař, V., Zhong, S., and Rasheed, F., "New Fluidic-Oscillator Concept for Flow-Separation Control". AIAA. J., 2013, 51(2), 379-405.
30. Tesař, V., "Impinging Jets". In: New, D. T. H. & Yu, S. C. M. (eds.) Vortex Rings and Jets: Recent Developments in Near-Field Dynamics. Singapore: Springer Singapore, 2015.
31. Thurman D, Poinsatte P, Ameri A, Culley D, Raghu S, Shyam V. "Investigation of Spiral and Sweeping Holes." ASME. Journal of Turbomachinery. 2016;138(9):091007-091007-11.
32. Wen, X., Tang, H., and Duan, F., Vortex dynamics of in-line twin synthetic jets in a laminar boundary layer. Physics of Fluids, 2015, 27(8): p.083601.
33. Willert, C.E., and Gharib, M., "Digital particle image velocimetry," Experiments in Fluids, 1991, 10(4): p.181-193.
34. Woszidlo, R., Ostermann, F., Nayeri, C. N., and Paschereit, C. O. "The time-resolved natural flow field of a fluidic oscillator," Experiments in Fluids, 2015, 56(6): p.125.
35. Yasuhiko, S., Shigeru, N., Taketoshi, O., and Koji, O., "A highly accurate iterative PIV technique using a gradient method," Measurement Science and Technology, 2000, 11(12): p.1666.

Figure captions

Figure 1 Sketch of the fluidic oscillator and its sweeping motion (not in scale, all dimensions in mm).

Figure 2 Sketch of experimental setup (not in scale).

Figure 3 Phase-averaged flow field. The black dots indicate the sampling locations to identify the phase angle of each individual PIV snapshot. The horizontal black line indicates the exit of jet nozzle. The light blue arc indicates the location where to extract the jet deflection angle and jet properties.

Figure 4 Period identification from an improved reference signal. (a) Differential values of transverse velocities at two positions symmetrical to the centerline of the flow field in the near-exit region. (b) Period identification based on correlation method.

Figure 5 (a) The jet's maximum deflection angle θ_{max} with error bar (uncertainty is obtained based on spatial resolution of PIV measurement) versus Reynolds number, and (b) Strouhal number Sh versus Reynolds number.

Figure 6 (a) Time-resolved deflection angle, (b) jet properties near the exit (peak jet velocity, jet width, and mass flow rate), at Reynolds number $Re = 4.0 \times 10^3$.

Figure 7 (a) Time-resolved deflection angle, (b) jet properties near the exit(peak jet velocity, jet width, and mass flow rate), at Reynolds number $Re = 9.3 \times 10^3$.

Figure 8 Instantaneous flow structures visualized by LIF at Reynolds number $Re = 4.0 \times 10^3$.

Figure 9 Instantaneous flow structures visualized by LIF at Reynolds number $Re = 9.3 \times 10^3$.

Figure 10 Phase-averaged flow fields at $Re = 4.0 \times 10^3$, from top to bottom: axial velocity, transverse velocity, vorticity, velocity fluctuating components along axial and transverse directions.

Figure 11 Phase-averaged velocity magnitude at $\beta / \pi = -1/9$ along four transvers lines at locations with different distance from impingement plate at $Re = 4.0 \times 10^3$.

Figure 12 Contour of phase-averaged axial velocity at $Re = 4.0 \times 10^3$ in two phase-symmetric position, left part at $\beta / \pi = -1/9$ and right part at $\beta / \pi = 8/9$.

Figure 13 Phase-averaged flow fields at $Re = 9.3 \times 10^3$, from top to bottom: axial velocity, transverse velocity, vorticity, velocity fluctuating components along axial and transverse directions.

Figure 14 Time-averaged velocity speed along the centerline ($y = 0$) at two selected Reynolds numbers.

Figure 15 Time-averaged *axial* (left) and *transverse* (right) velocity components (a), and velocity fluctuating components (b), at the near-exit region ($x = 3.4d_h$) and near-wall region ($x = 7.7d_h$) at two selected Reynolds numbers.

Figure 16 (a) Imaginary versus real parts of eigenvalues at $Re = 4.0 \times 10^3$, (b) energy and frequency captured in each DMD mode (size of the solid cycle indicates the captured fluctuating energy), (c-d) flow structures of the first two DMD modes (the real part is on the left, the imaginary part is on the right).

Figure 17 Phase correlation map of the first two DMD mode coefficients of the real part at $Re = 4.0 \times 10^3$.

Figure 18 Temporal variations of the most energetic flow structures at $Re = 4.0 \times 10^3$. (a) phase-averaged flow fields at three phase angles; (b-c) flow structures captured by each DMD mode pair at the three phase angles.

Figure 19 (a) Imaginary versus real parts of eigenvalues at $Re = 9.3 \times 10^3$, (b) energy and frequency captured in each DMD mode (size of the solid cycle indicates the captured fluctuating energy), (c-d) flow structures of the first two DMD modes (the real part is on the left, the imaginary part on the right).

Figure 20 Phase correlation map of the first two DMD mode coefficients of the real part at $Re = 9.3 \times 10^3$.

Figure 21 Temporal variations of the most energetic flow structures at $Re = 9.3 \times 10^3$. (a) Phase-averaged flow fields at three phase angles; (b-c) the flow structures captured by each DMD mode pair at the three phase angles.

Table caption

Table 1 Tested flow rates with corresponding jet velocity and Reynolds numbers.

Figure 1

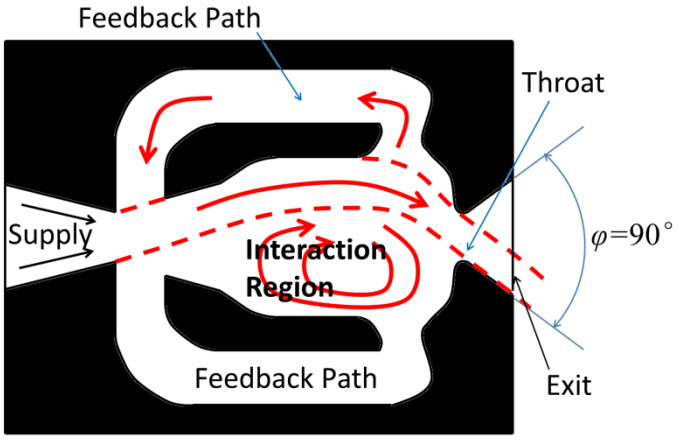

(a) phase 1

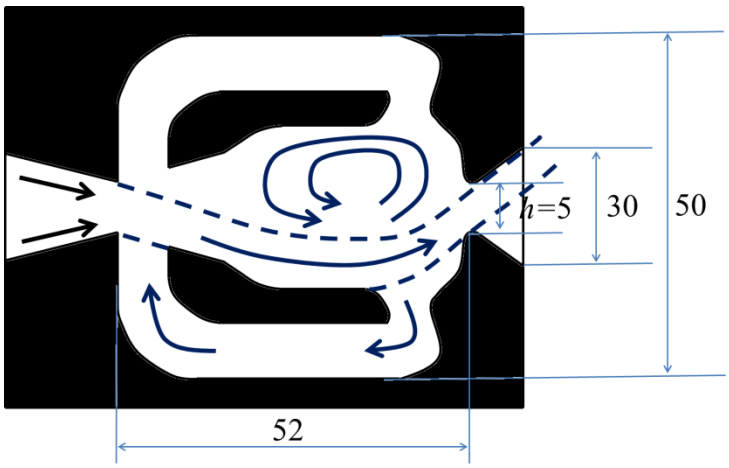

(b) phase 2

Sketch of the fluidic oscillator and its sweeping motion (not in scale, all dimensions in mm).

Figure 2

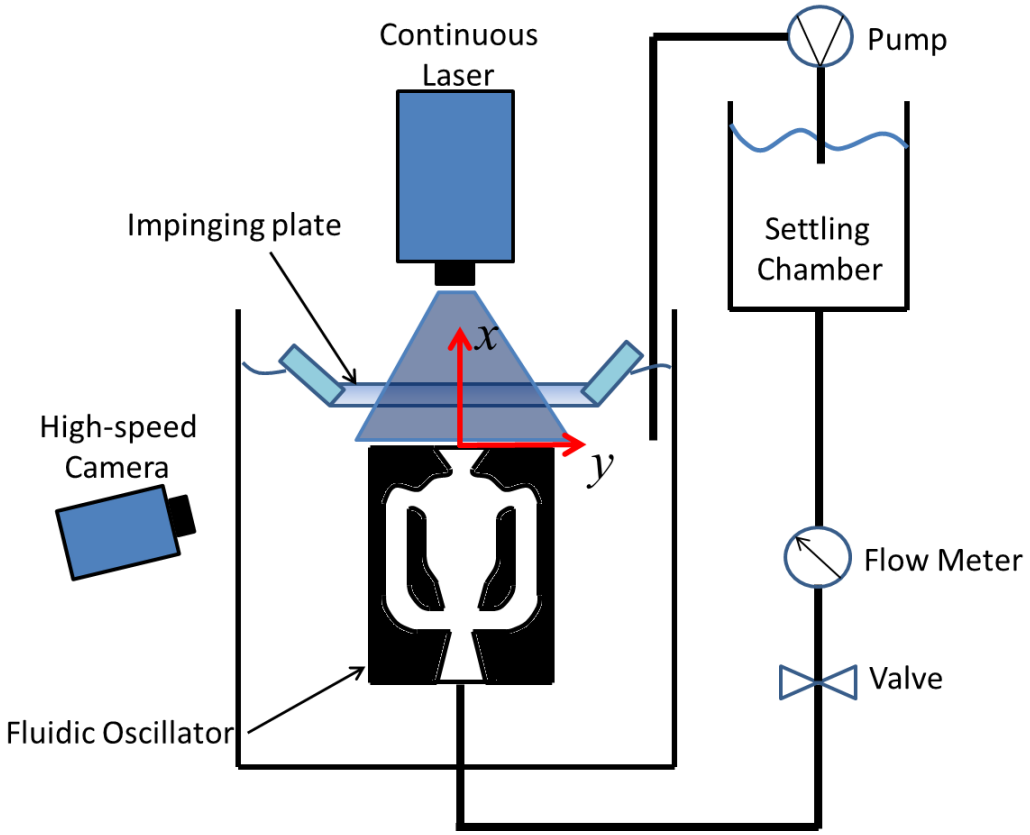

Sketch of experimental setup (not in scale).

Figure 3

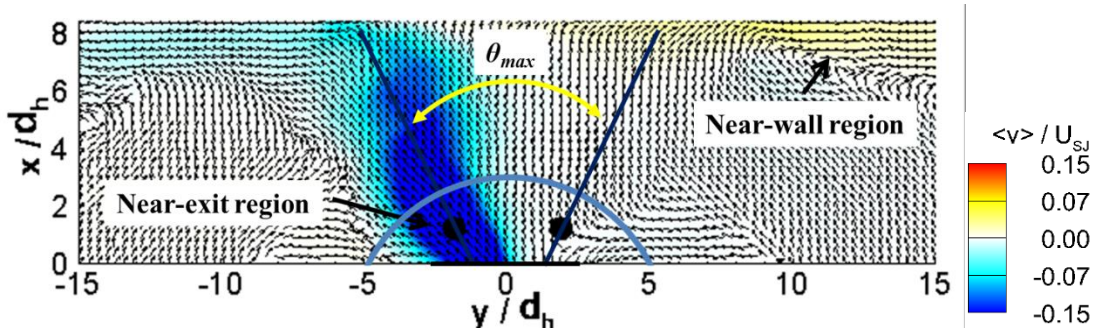

Phase-averaged flow field. The black dots indicate the sampling locations to identify the phase angle of each individual PIV snapshot. The horizontal black line indicates the exit of jet nozzle. The light blue arc indicates the location where to extract the jet deflection angle and jet properties.

Figure 4

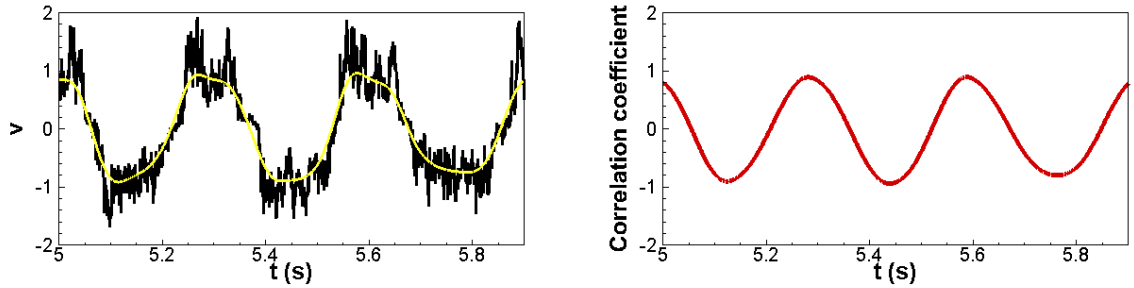

(a) (b)

Period identification from an improved reference signal. (a) Differential values of transverse velocities at two positions symmetrical to the centerline of the flow field in the near-exit region. (b) Period identification based on correlation method.

Figure 5

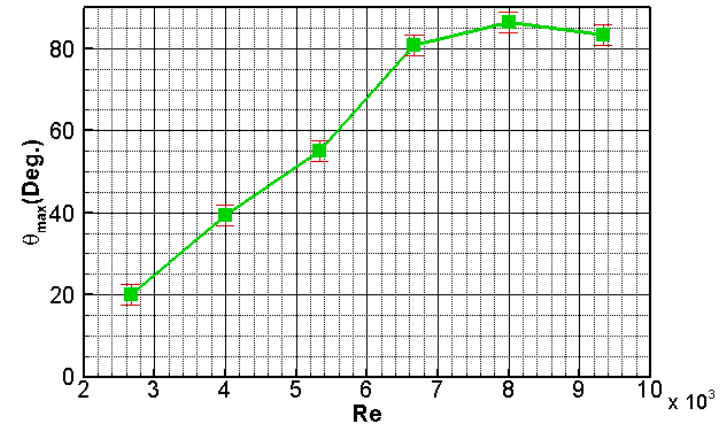

(a)

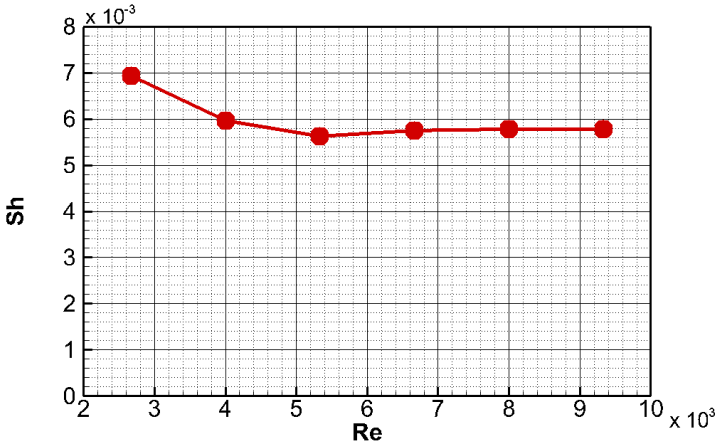

(b)

(a) The jet's maximum deflection angle θ_{max} with error bar (uncertainty is obtained based on spatial resolution of PIV measurement) versus Reynolds number, and (b) Strouhal number Sh versus Reynolds number.

Figure 6

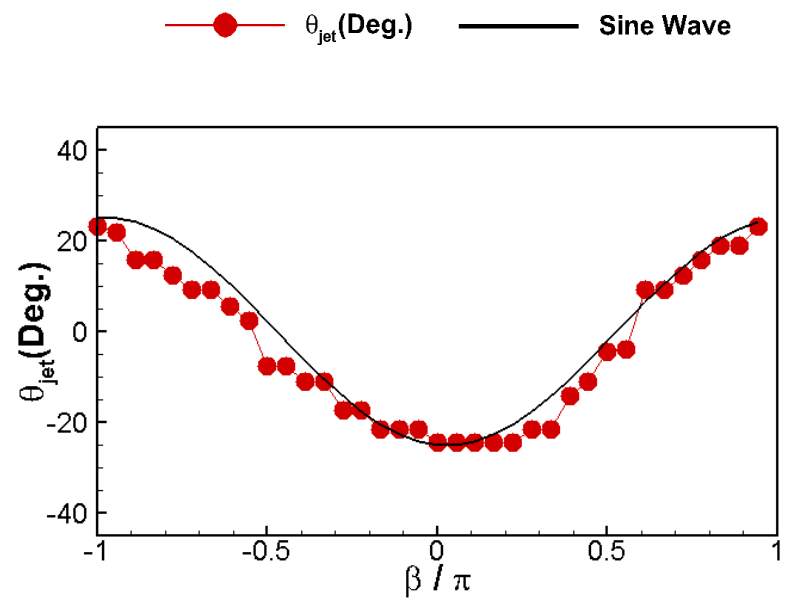

(a)

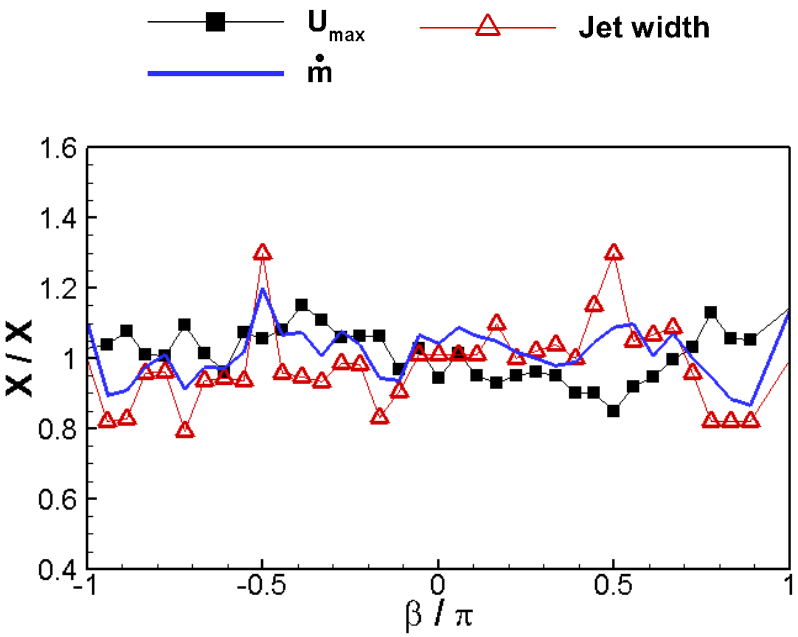

(b)

(a) Time-resolved deflection angle, (b) jet properties near the exit (peak jet velocity, jet width and mass flow rate), at Reynolds number $Re = 4.0 \times 10^3$.

Figure 7

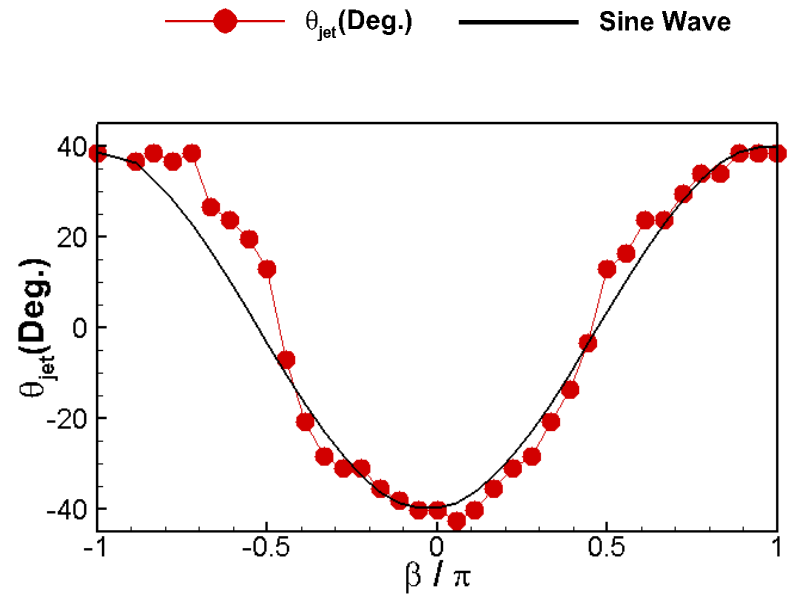

(a)

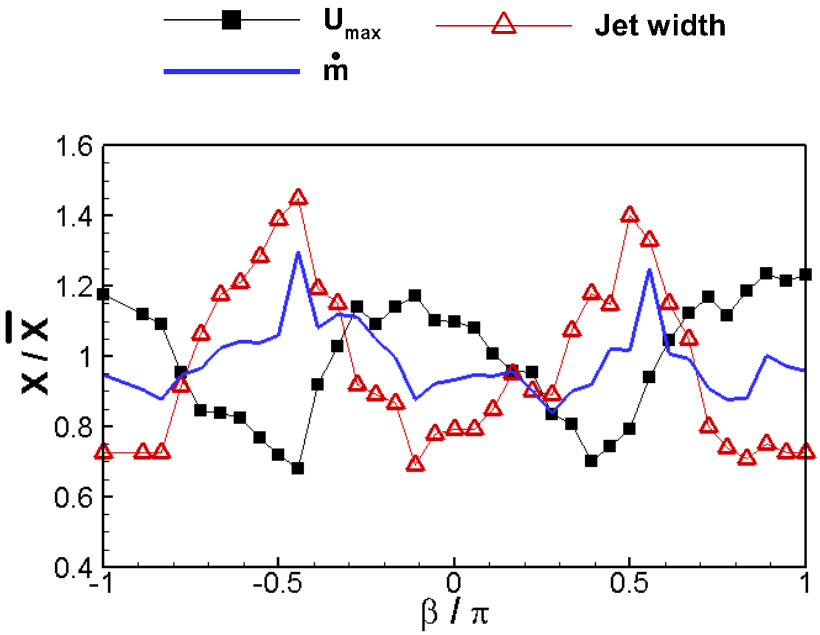

(b)

(a) Time-resolved deflection angle, (b) jet properties (peak jet velocity, jet width and mass flow rate) near the exit, at Reynolds number $Re = 9.3 \times 10^3$.

Figure 8

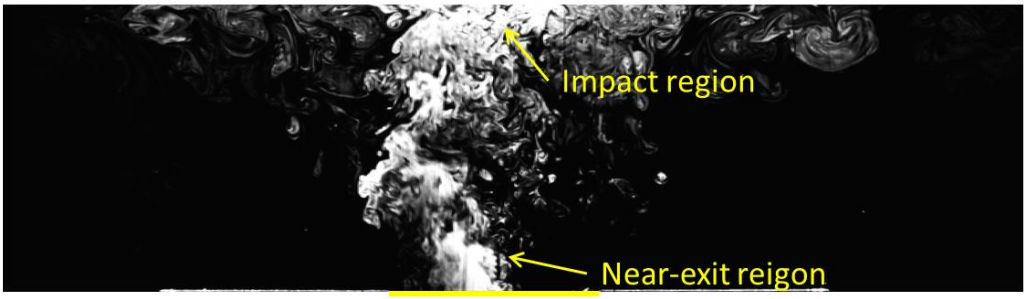

(a) β / π = -1/9

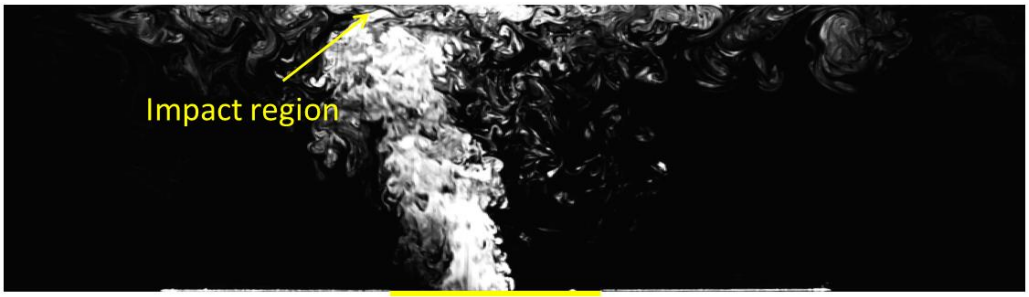

(b) β / π = 2/9

(c) β / π = 5/9

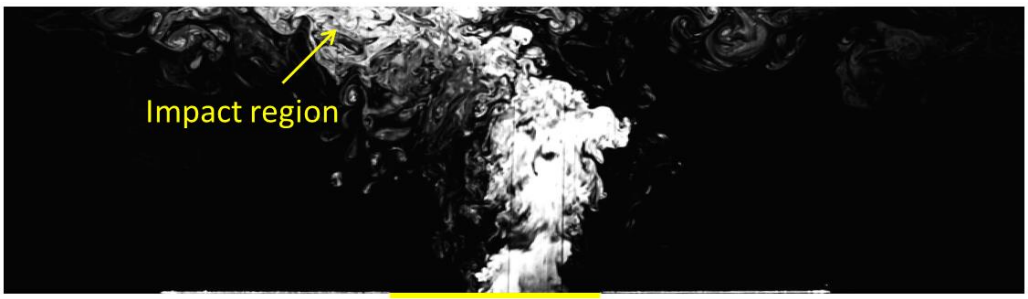

(d) β / π = 8/9

Instantaneous flow structures visualized by LIF at Reynolds number $Re = 4.0 \times 10^3$.

Figure 9

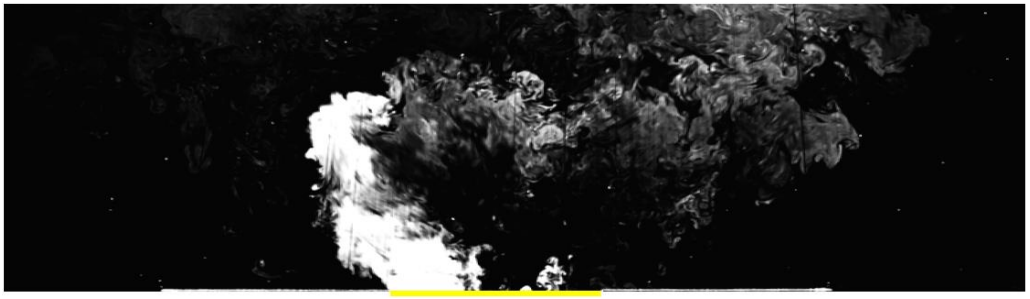

(a) $\beta / \pi = -1/9$

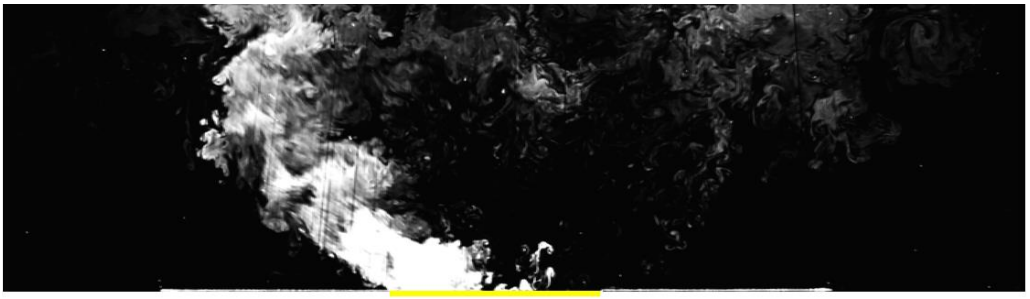

(b) $\beta / \pi = 2/9$

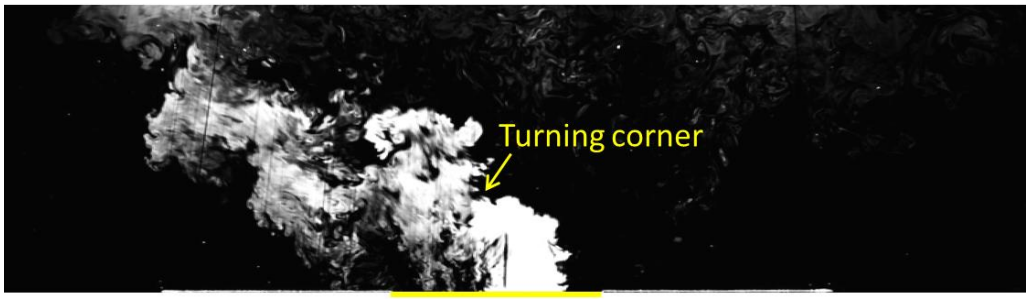

(c) $\beta / \pi = 5/9$

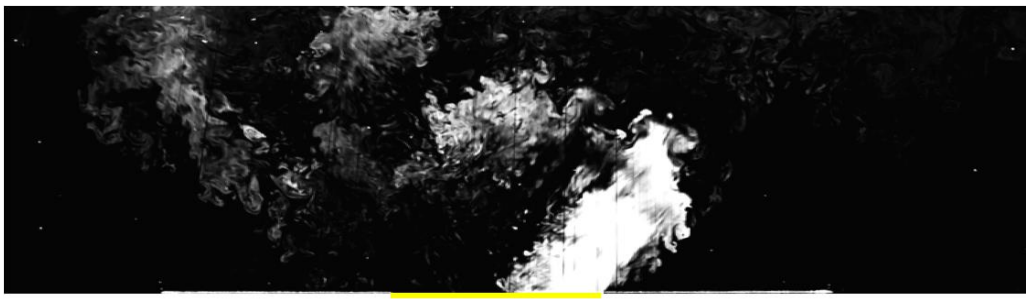

(d) $\beta / \pi = 8/9$

Instantaneous flow structures visualized by LIF at Reynolds number $Re = 9.3 \times 10^3$.

Figure 10

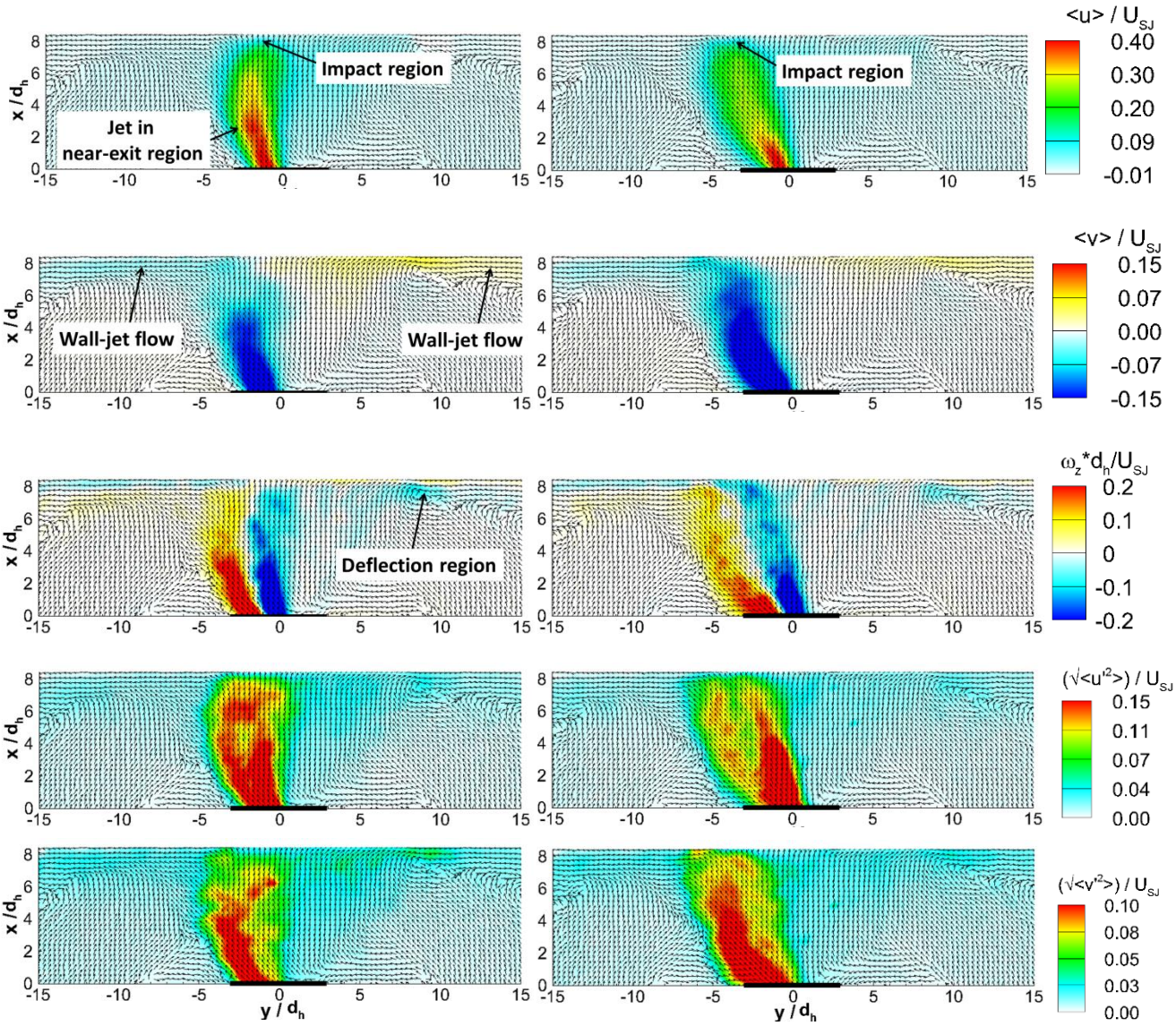

(a) β / π = -1/9 (b) β / π = 2/9

Figure 10-continued

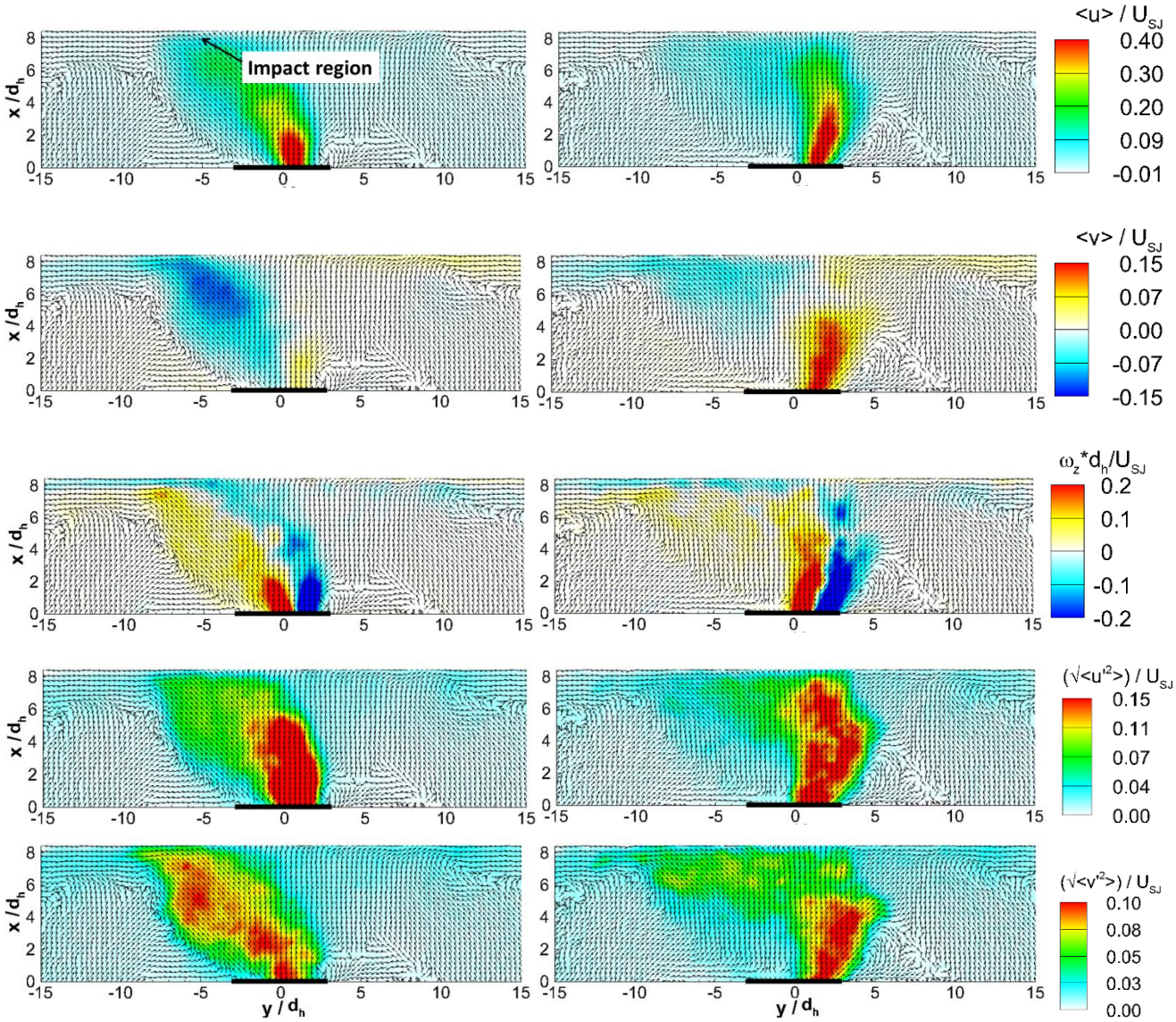

(c) $\beta / \pi = 5/9$ (d) $\beta / \pi = 8/9$

Phase- averaged flow fields at $Re = 4.0 \times 10^3$, from top to bottom: axial velocity, transverse velocity, vorticity, velocity fluctuating components along axial and transverse directions.

Figure 11

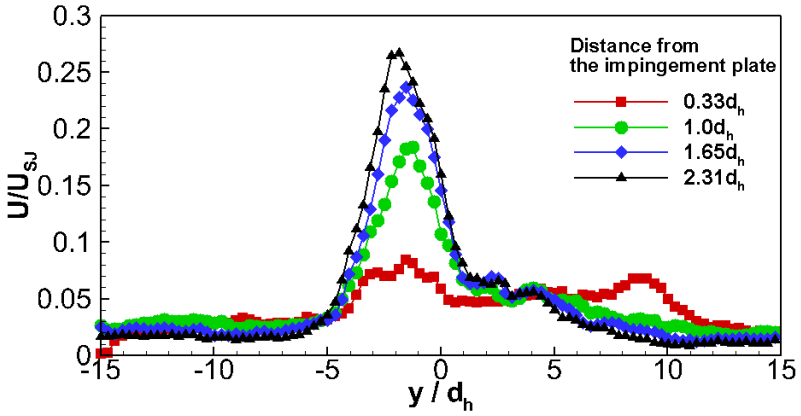

Phase-averaged velocity magnitude at $\beta / \pi = -1/9$ along four transvers lines at different distance from impingement plate at $Re = 4.0 \times 10^3$.

Figure 12

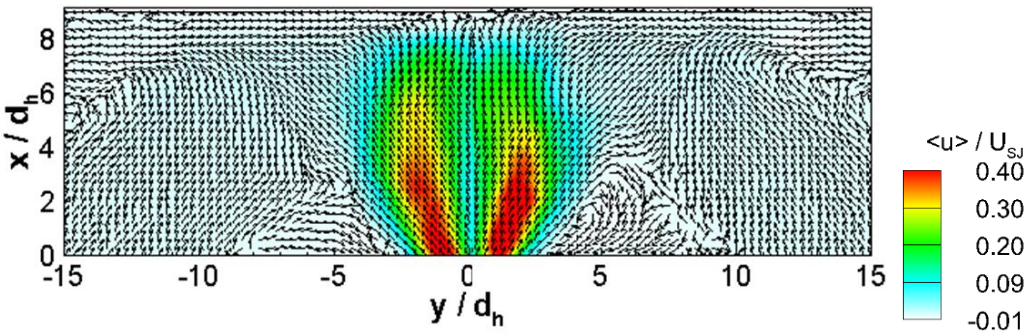

Contour of phase-averaged axial velocity at $Re = 4.0 \times 10^3$ at two phase-symmetric positions, left part at $\beta / \pi = -1/9$ and right part at $\beta / \pi = 8/9$

Figure 13

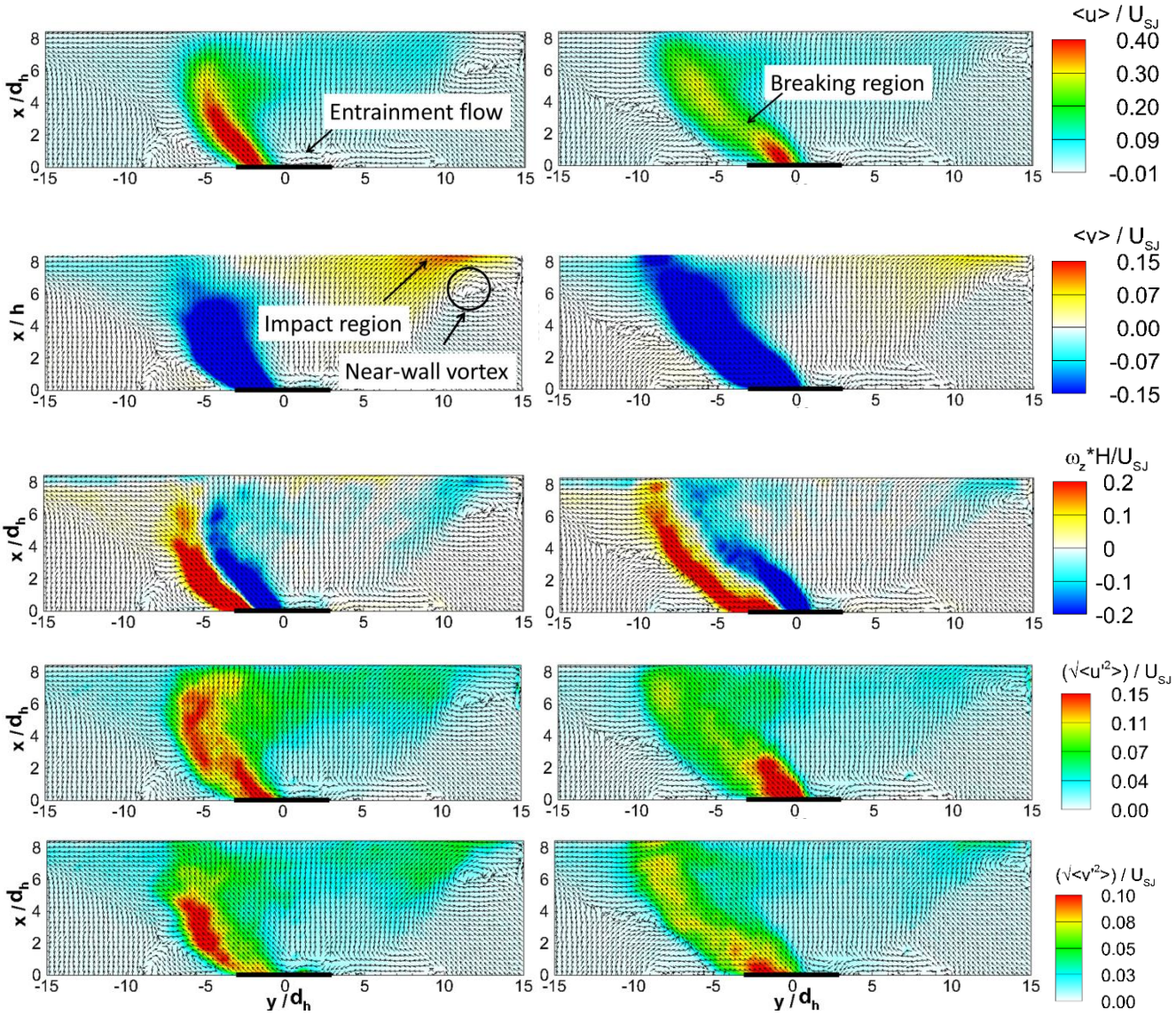

(a) β / π = -1/9 (b) β / π =2/9

Figure 13- continued

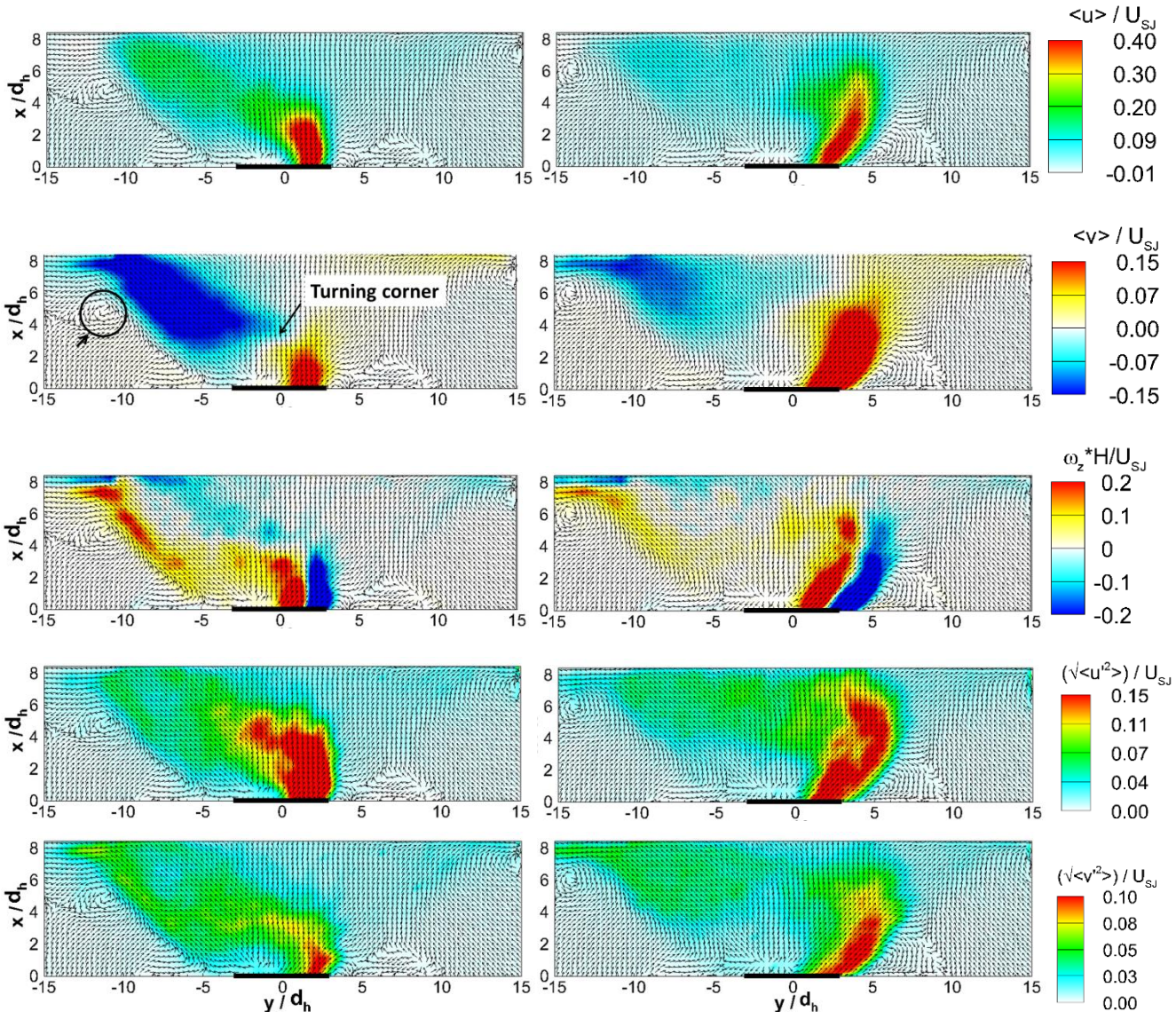

(c) $\beta / \pi = 5/9$ (d) $\beta / \pi = 8/9$

Phase averaged flow fields at $Re = 9.3 \times 10^3$, from top to bottom: axial velocity, transverse velocity, vorticity, velocity fluctuating components along axial and transverse directions.

Figure 14

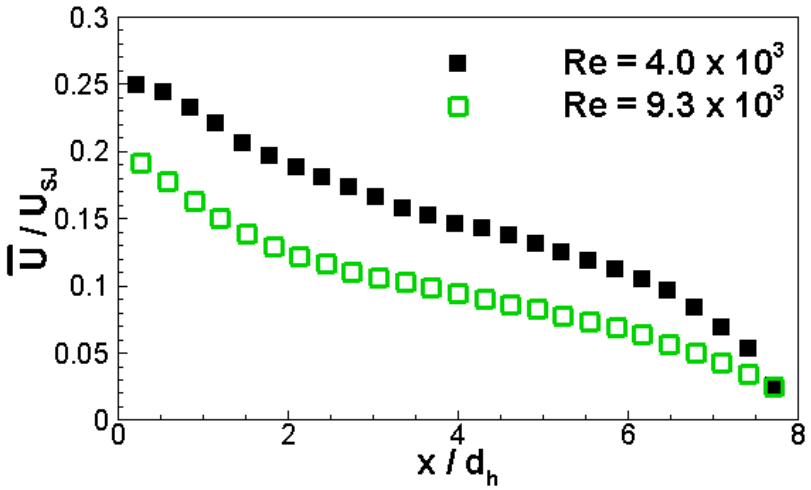

Time-averaged velocity speed along the centerline ($y = 0$) at two selected Reynolds numbers.

Figure 15

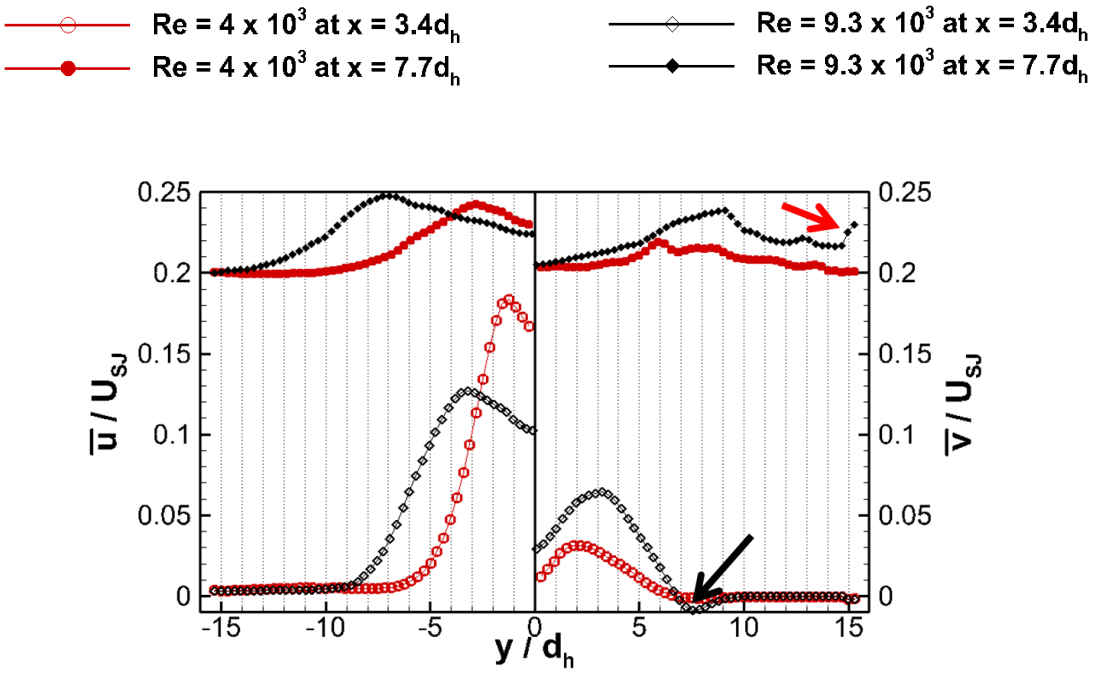

(a) values at $x = 7.7d_h$ are shifted by 0.2.

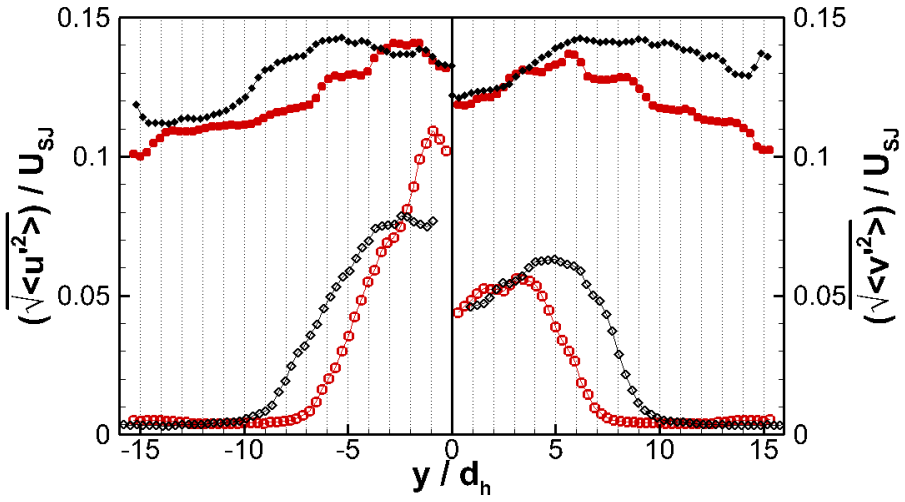

(b) values at $x = 7.7d_h$ are shifted by 0.1.

Time-averaged *axial* (left) and *transverse* (right) velocity components (a), and velocity fluctuating components (b), along two transverse lines in the near-exit region ($x = 3.4d_h$) and near-wall region ($x = 7.7d_h$) at two selected Reynolds numbers.

Figure 16

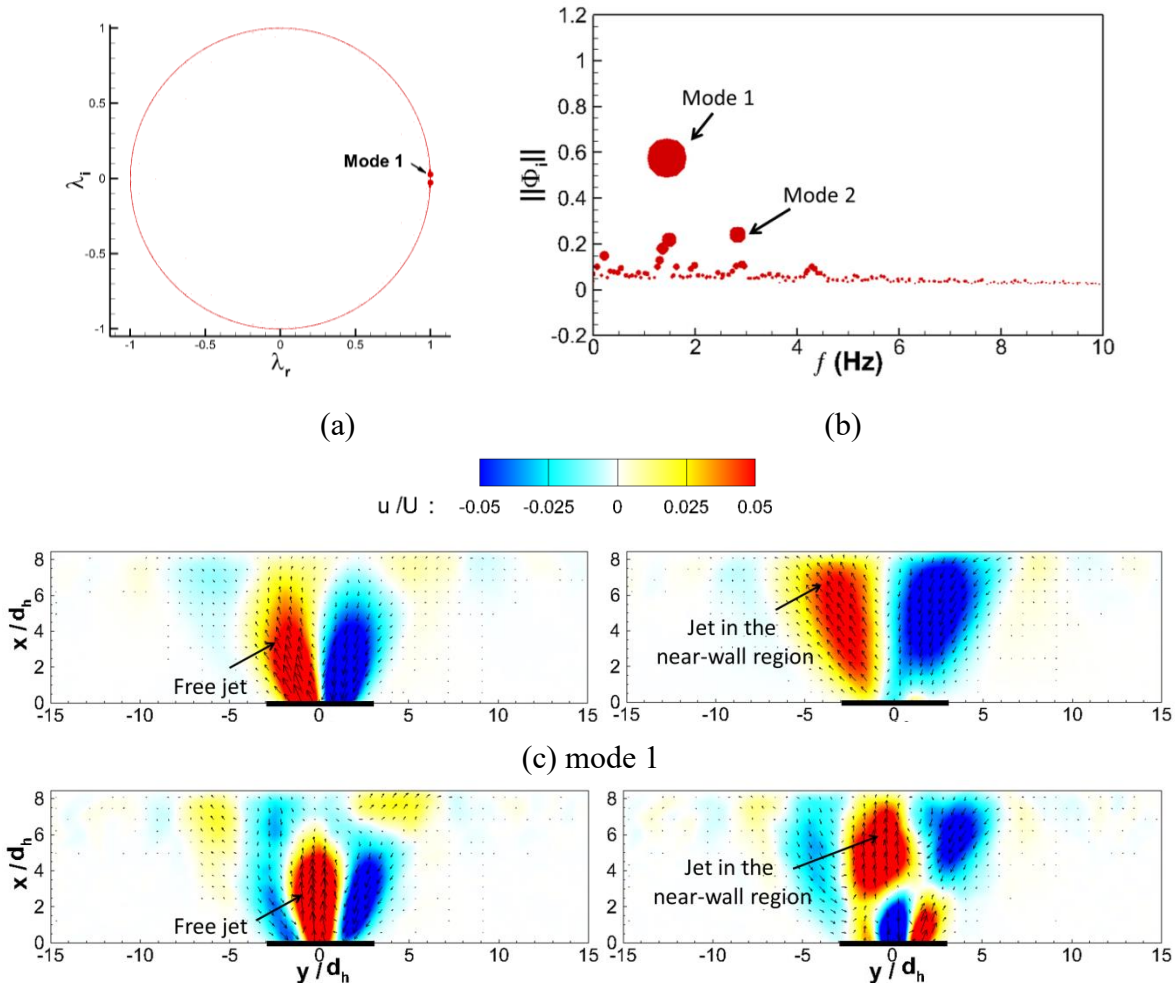

(a) Imaginary versus real parts of eigenvalues at Re = 4.0×10^3, (b) energy and frequency captured in each DMD mode (size of the solid cycle indicates the captured fluctuating energy), (c-d) flow structures of the first two DMD modes (the real part is on the left, the imaginary part is on the right).

Figure 17

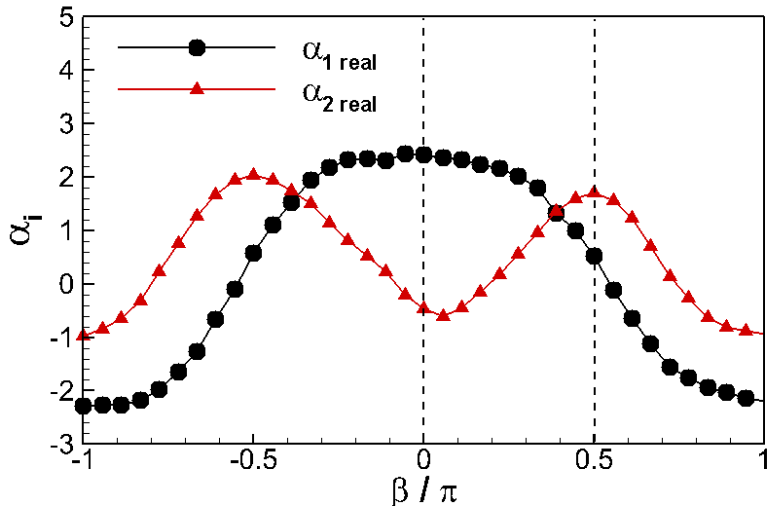

Phase correlation map of the first two DMD mode coefficients of the real part at $Re = 4.0 \times 10^3$.

Figure 18

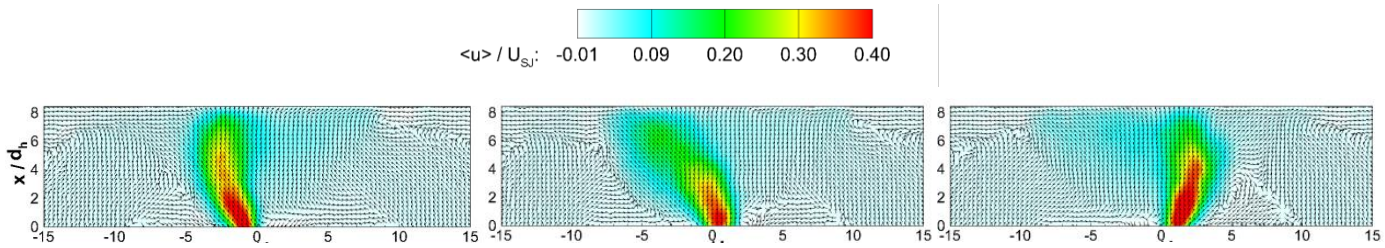

$\beta / \pi = 0$ $\beta / \pi = 1/2$ $\beta / \pi = 1$

(a) Contour of phase-averaged axial velocity and velocity vectors

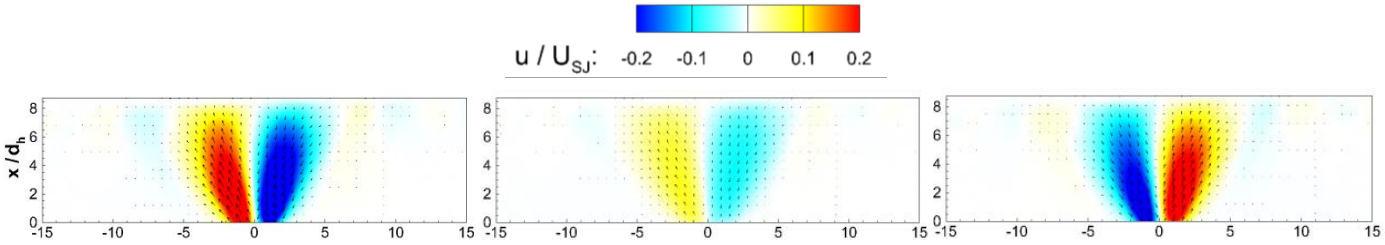

$\beta / \pi = 0$ $\beta / \pi = 1/2$ $\beta / \pi = 1$

(b) mode 1

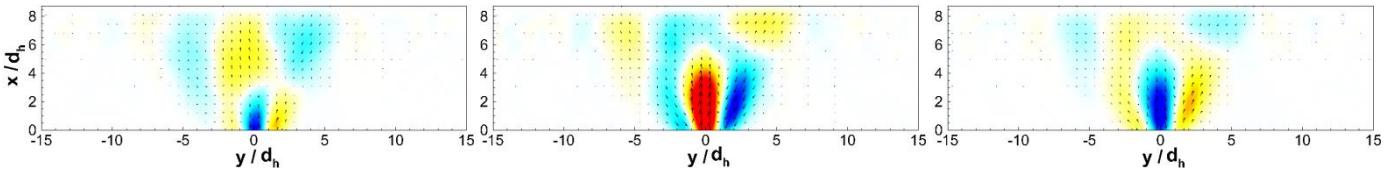

$\beta / \pi = 0$ $\beta / \pi = 1/2$ $\beta / \pi = 1$

(c) mode 2

Temporal variations of the most energetic flow structures at $Re = 4.0 \times 10^3$, (a) phase-averaged flow fields at three phase angles, (b-c) flow structures captured by each DMD mode pair at the three phase angles.

Figure 19

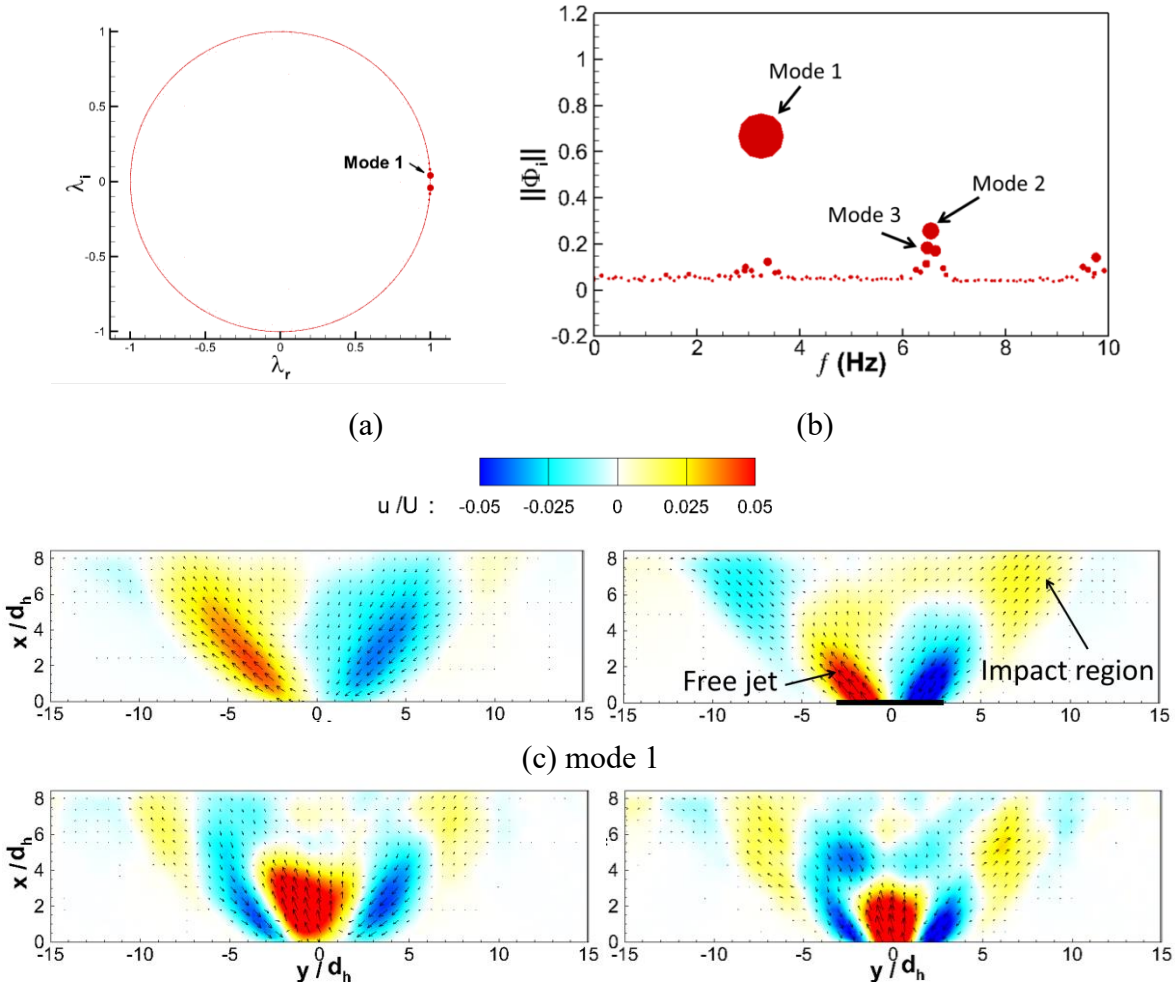

(a) Imaginary versus real parts of eigenvalues at Re = 9.3×10^3, (b) energy and frequency captured in each DMD mode (size of the solid cycle indicates the captured fluctuating energy), (c-d) flow structures of the first two DMD modes (the real part is on the left, the imaginary part is on the right).

Figure 20

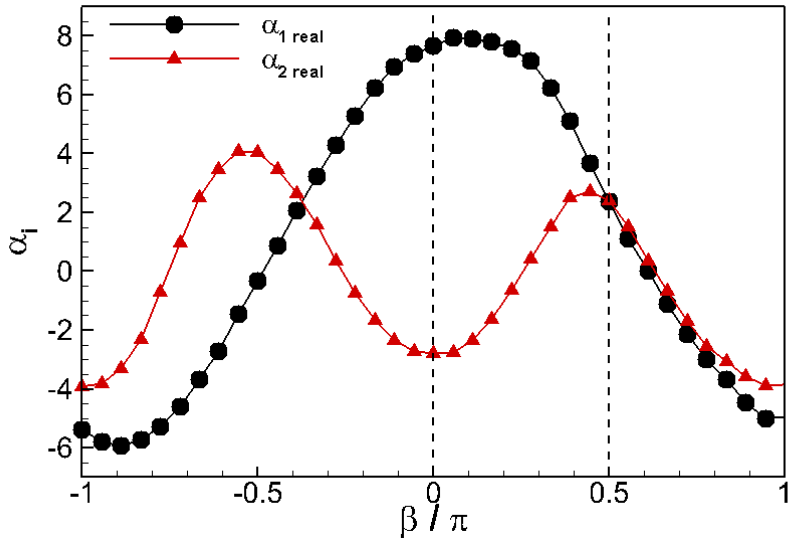

Phase correlation map of the first two DMD mode coefficients of the real part at $Re = 9.3 \times 10^3$.

Figure 21

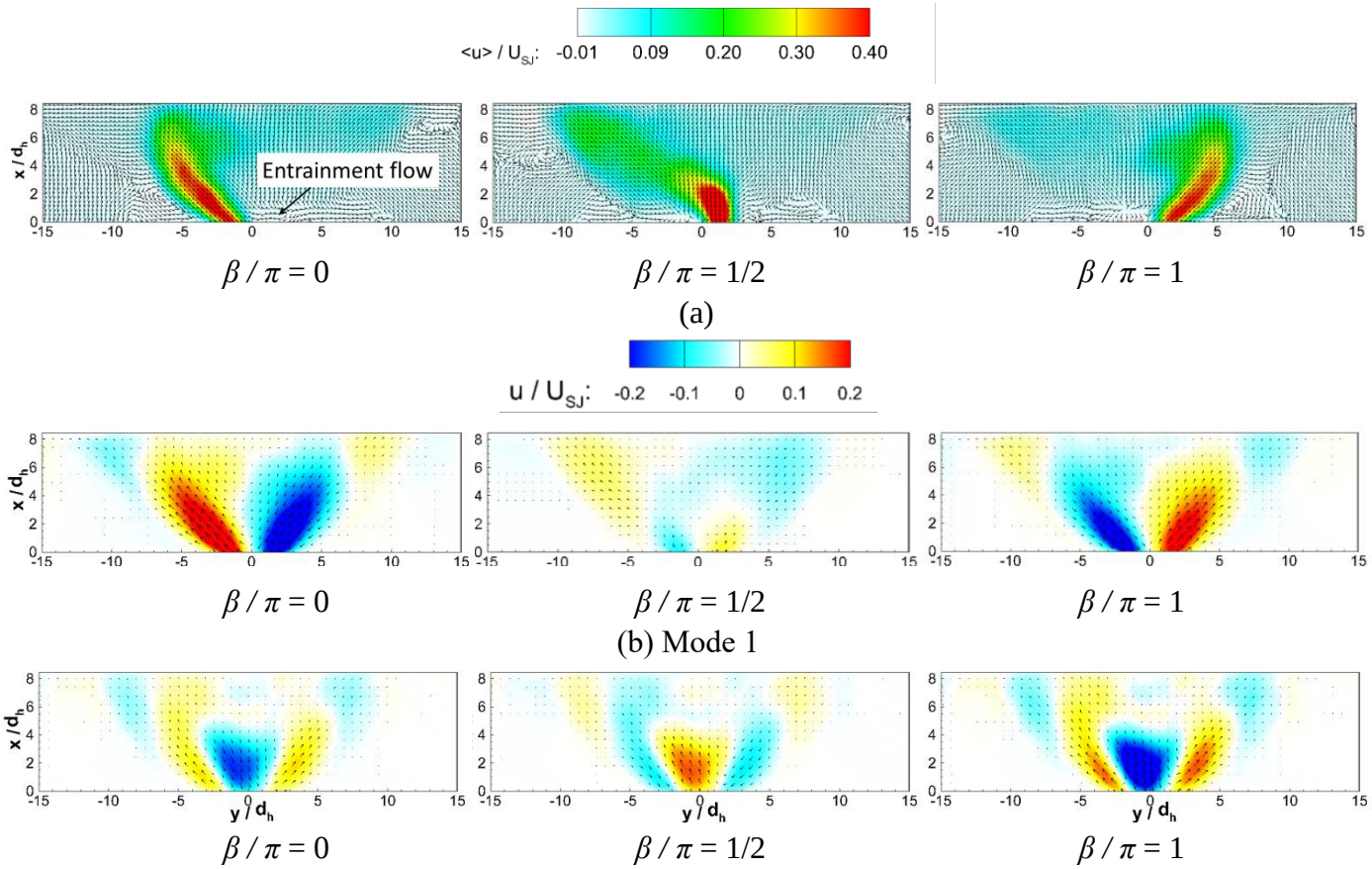

Temporal variations of the most energetic flow structures at $Re = 9.3 \times 10^3$, (a) phase-averaged flow fields at three phase angles, (b-c) flow structures captured by each DMD mode pair at the three phase angles.

Table 1

Tested flow rates with corresponding jet velocity and Reynolds numbers

Volume flow ($10^{-6}m^3/s$)	Sweeping jet velocity U_{SJ} (m/s)	Reynolds number Re ($\times 10^3$) based on d_h
13.3	0.53	2.6
20	0.8	4.0
26.7	1.07	5.3
33.3	1.33	6.7
40	1.6	8.0
46.7	1.87	9.3